

Chaos as a Possible Probe for Scalar Hair in Horndeski Gravity

Yang Yu^{1,*}, Ruo-Ting Chen^{1,†}, Shulan Li^{2,‡}, Dan Zhang^{1,§} and Jian-Pin Wu^{1,¶}

¹ *Center for Gravitation and Cosmology, College of Physical Science and Technology,
Yangzhou University, Yangzhou 225009, China*

² *Department of Physics, Shanghai University, Shanghai 200444, China*

Abstract

The detection of black hole scalar hair, a possible deviation from general relativity’s “no-hair” theorem, requires sensitive probes beyond conventional methods. This study proposes chaotic dynamics as a novel indicator for scalar hair in Horndeski gravity. We investigate the motion of a spinning test particle in a static, spherically symmetric hairy black hole spacetime. Our results show that increasing scalar hair systematically suppresses orbital chaos, as evidenced by regularized precession, reduced Lyapunov exponents, and contracted Poincaré sections. Furthermore, scalar hair enhances the correlation between the two gravitational wave polarization modes, restoring phase coherence. These findings demonstrate that chaotic observables and gravitational wave signatures can jointly serve as sensitive probes for black hole hair, offering a complementary approach to testing gravity in strong-field regimes.

*mx120230358@stu.yzu.edu.cn

†ruotingchen@163.com

‡shulanli.yzu@gmail.com

§danzhanglnk@163.com

¶jianpinwu@yzu.edu.cn

Contents

I. Introduction	3
II. Spinning Particle Dynamics in a Hairy Spacetime	4
A. Horndeski Theory and the Hairy BH Solution	5
B. MPD Equations	6
C. Initial Conditions	7
D. Orbital Dynamics	10
III. Effective Potential Analysis	14
A. Effective Potential	15
B. Effective Potential Metaphor and Saddle Points	17
IV. Chaotic Dynamics Analysis	19
A. Takens' Embedding Theory	20
B. Wolf Algorithm for LEs	21
C. Indicators of Chaotic Dynamics	22
V. Gravitational Waveform	23
A. Quadrupole Formula	23
B. Gravitational Waveform Signatures	26
C. Observational Time Scales	31
VI. Conclusions and Discussions	32
Acknowledgments	33
A. Energy and Angular Momentum in Terms of Orbital Parameters	34
B. The Poincaré Section in An Extremely Long Time Evolution	36
References	36

I. INTRODUCTION

The “no-hair theorem”, formulated in the early 1970s, posits that an isolated, stationary black hole (BH) in general relativity (GR) is uniquely characterized by only three classical parameters: mass, electric charge, and angular momentum [1–5]. This profound result implies that all other information about the progenitor matter that formed the BH or fell into it—the “hair”—is irretrievably lost behind the event horizon. While this theorem holds rigorously in vacuum Einstein-Maxwell theory, its validity in more general gravitational frameworks remains a subject of intense investigation. Numerous counterexamples and extensions have been explored, particularly in theories involving scalar fields, leading to the concept of “hairy” BHs. A particularly fertile framework for such solutions is Horndeski gravity, the most general scalar-tensor theory with second-order equations of motion. Horndeski theories not only provide a consistent platform for infrared modifications of gravity, potentially addressing late-time cosmic acceleration, but also admit exact, asymptotically flat BH solutions endowed with nontrivial scalar hair [6].

Despite the theoretical appeal of hairy BHs, any viable modified gravity theory faces stringent empirical constraints. A wealth of experiments—from solar system tests [7] to binary pulsar dynamics and gravitational wave (GW) observations [8–10]—have consistently confirmed GR’s remarkable accuracy, particularly within the well-tested weak-field regime. Even in the strong-field regime, deviations from GR, such as those induced by scalar hair, are expected to be exceedingly faint. Detecting these subtle signatures therefore demands exceptionally sensitive probes.

Chaotic dynamical systems, renowned for their sensitivity to initial conditions and parameter variations, offer a promising avenue for such high-precision tests. In GR, the integrability of geodesic motion can be broken by additional degrees of freedom, such as particle spin. As demonstrated by Suzuki and Maeda [11], a spinning test particle in Schwarzschild spacetime can exhibit chaotic motion beyond a critical spin, governed by the Mathisson-Papapetrou-Dixon (MPD) equations [12–14]. This chaos originates from saddle points in the effective potential, leading to heteroclinic orbits and is quantifiable via positive Lyapunov exponents (LEs) and broken tori in Poincaré sections. The orbital dynamics of stars or compact objects near supermassive BHs, such as the S-stars orbiting Sgr A*, thus constitute a natural laboratory where minute metric deviations could be amplified through chaotic

evolution, imprinting on both trajectories and GW emissions.

Recent advances in observational techniques—from the optical imaging by the Event Horizon Telescope [15–25] to the detection of GWs [8–10, 26–31]—have opened new windows onto strong-field gravity. Concurrently, efforts to constrain or detect BH hair through these channels are actively underway [32–36]. Building on these developments, we propose that the chaotic dynamics of spinning particles can serve as a complementary and highly sensitive probe for scalar hair.

In this work, we study the chaotic dynamics of a spinning test particle, governed by the MPD equations, in the hairy BH spacetime of Horndeski gravity. Our primary goal is to investigate how the scalar hair influences the onset and characteristics of the chaos, and to assess the potential of chaotic observables as discriminators between GR and its extensions. We compute LEs and Poincaré maps across a range of hairy parameters, demonstrating that chaos is not only modulated but can also be suppressed by the presence of scalar hair. Furthermore, we extend our analysis to the gravitational waveform emitted by the chaotic orbiting particle, constructed via the quadrupole formula, and examine distinctive modifications induced by the scalar hair.

This paper is organized as follows. Sec. II introduces the Horndeski gravity framework and hairy BH solutions, derives the MPD equations for spinning test particles, specifies the initial conditions, and numerically analyzes the orbital dynamics. Sec. III investigates the effective potential, classifying its types and elucidating the role of saddle points in mediating chaotic behavior. Sec. IV analyzes chaotic dynamics, employing Takens’ embedding theory for phase space reconstruction, the Wolf algorithm to compute LEs, and Poincaré sections to quantify how scalar hair suppresses chaos. Sec. V extends the analysis to GW signatures, constructing waveforms via the quadrupole formula, quantifying phase coherence between polarization modes, and estimating observational time scales for detectability. Finally, Sec. VI summarizes the key findings, highlights the complementary roles of chaotic dynamics and GWs in probing scalar hair, and suggests future research directions.

II. SPINNING PARTICLE DYNAMICS IN A HAIRY SPACETIME

In this section, we investigate the orbital dynamics governed by the MPD equations in the hairy BH spacetime of Horndeski gravity. A brief review of the hairy BH solution in

this theory is provided in subsection II A. In subsection II B, we derive the corresponding MPD equations that govern the motion of a spinning test particle, and in subsection II C we specify the necessary initial conditions. Finally, we numerically integrate the MPD equations in the hairy BH background and analyze the characteristics of the resulting orbital motion in subsection II D.

A. Horndeski Theory and the Hairy BH Solution

We consider the most general scalar-tensor theory yielding second-order equations of motion in 4 dimensions, namely the Horndeski theory. Its action can be written as [37, 38]

$$S = \int d^4x \sqrt{-g} [Q_2 + Q_3 \square\varphi + Q_4 R + Q_{4,\chi} ((\square\varphi)^2 - (\nabla^\mu \nabla^\nu \varphi)(\nabla_\mu \nabla_\nu \varphi)) + Q_5 G_{\mu\nu} \nabla^\mu \nabla^\nu \varphi - \frac{1}{6} Q_{5,\chi} ((\square\varphi)^3 - 3(\square\varphi)(\nabla^\mu \nabla^\nu \varphi)(\nabla_\mu \nabla_\nu \varphi) + 2(\nabla_\mu \nabla_\nu \varphi)(\nabla^\nu \nabla^\gamma \varphi)(\nabla_\gamma \nabla^\mu \varphi)], \quad (1)$$

where φ is the scalar field, $\chi = -\frac{1}{2}\partial^\mu\varphi\partial_\mu\varphi$ denotes its kinetic term, Q_i ($i = 2, 3, 4, 5$) are arbitrary functions of χ , R and $G_{\mu\nu}$ are the Ricci scalar and the Einstein tensor respectively, and $Q_{i,\chi}$ stands for the derivative of Q_i with respect to χ [37]. This theory encompasses a broad class of modified gravity models while preserving second-order equations of motion, thereby avoiding Ostrogradsky ghosts.

In the present work [38], the authors focus on a specific subclass of quartic Horndeski theory, corresponding to the choice $Q_5 = 0$. In this case, the field equations admit static, spherically symmetric BH solutions endowed with scalar hair. Following Ref. [38], we work with geometric units $G = c = 1$, and the solution in Schwarzschild coordinates is given by

$$ds^2 = -f(r)dt^2 + f^{-1}(r)dr^2 + r^2d\Omega^2, \quad (2a)$$

$$f(r) = 1 - \frac{2M}{r} - \frac{h}{r} \ln \frac{r}{2M}, \quad (2b)$$

$$d\Omega^2 = d\theta^2 + \sin^2\theta d\phi^2, \quad (2c)$$

where h is a parameter that encodes the imprint of the scalar field outside the horizon, i.e., the ‘‘hair’’. For $h = 0$, the metric (2) reduces to the standard Schwarzschild solution. This family of solutions evades the classical no-hair theorem by relaxing some of its underlying assumptions. In particular, it ignores the kinetic term χ and considers a non-minimal coupling between the scalar field and curvature ($Q_4 R$), thereby allowing for a non-trivial

scalar configuration outside the event horizon. Consequently, the metric (2) provides a self-consistent, analytically tractable background for probing strong-field gravitational effects beyond GR. To simplify the analysis, we henceforth set the BH mass $M = 1$, which serves as our fundamental scale.

This solution has been extensively studied in several works, including investigations into the optical appearance of BHs in Ref. [39], the propagation of external fields in Ref. [40], and strong gravitational lensing effects in Ref. [41]. In parallel, the rotating form of Eq. (2), derived via the Newman-Janis algorithm (NJA), has also been widely examined in Refs. [42–46].

B. MPD Equations

The dynamics of a massive spinning particle in a curved spacetime is governed by MPD equations [12–14]. In covariant form, they read

$$u^\mu = \frac{dx^\mu}{d\tau}, \quad (3a)$$

$$\frac{Dp^\mu}{d\tau} = -\frac{1}{2}R^\mu{}_{\nu\alpha\beta}u^\nu S^{\alpha\beta}, \quad (3b)$$

$$\frac{DS^{\mu\nu}}{d\tau} = p^\mu u^\nu - p^\nu u^\mu, \quad (3c)$$

where τ is the proper time as an affine parameter along the particle’s worldline, u^μ is the 4-velocity, p^μ is the generalized 4-momentum, and $S^{\mu\nu} = -S^{\nu\mu}$ is the antisymmetric spin tensor. The curvature tensor of the background spacetime is denoted by $R^\mu{}_{\nu\rho\sigma}$. In the following calculations, we denote the derivatives of the proper time as a dot above the variables.

The system (3) is not closed because the relation between u^μ and p^μ is not specified. To close it one must impose a supplementary spin condition (SSC). Different SSCs correspond to different choices of the representative worldline that describes the center of mass [47]. In this work, we adopt the Tulczyjew-Dixon (TD) condition (known as TD-SSC), which provides a unique worldline [14, 48]

$$p_\mu S^{\mu\nu} = 0. \quad (4)$$

With this SSC, the 4-velocity can be expressed in terms of p^μ and $S^{\mu\nu}$ [49]:

$$u^\alpha = -\frac{p^\alpha u_\alpha}{m^2} \left(p^\alpha + \frac{1}{2} \frac{S^{\alpha\beta} R_{\gamma\beta\mu\nu} p^\gamma S^{\mu\nu}}{m^2 + R_{\mu\nu\rho\sigma} S^{\mu\nu} S^{\rho\sigma} / 4} \right). \quad (5)$$

Using TD-SSC, we can define the conserved mass of the particle m as:

$$m^2 = -p_\mu p^\mu. \quad (6)$$

For numerical integration, it is advantageous to replace the antisymmetric spin tensor $S^{\mu\nu}$ with a spin 4-vector, following the procedure in Ref. [50]:

$$S^\alpha = \frac{1}{2m} \varepsilon^\alpha{}_{\beta\mu\nu} p^\beta S^{\mu\nu}, \quad (7)$$

where $\varepsilon_{\alpha\beta\mu\nu} = \sqrt{-g} \sigma_{\alpha\beta\mu\nu}$ is the Levi-Civita tensor and $\sigma_{\alpha\beta\mu\nu}$ is the alternating symbol. The inverse relation is

$$S^{\alpha\beta} = \frac{1}{m} \varepsilon^{\alpha\beta\mu\nu} p_\mu S_\nu. \quad (8)$$

The magnitude of spin is conserved and can be written as

$$S^2 = S_\alpha S^\alpha = \frac{1}{2} S_{\mu\nu} S^{\mu\nu}. \quad (9)$$

Then the TD-SSC (4) with a spin vector becomes

$$p_\alpha S^\alpha = 0, \quad (10)$$

and the MPD equations with vector-form variables take a form ready for numerical integration:

$$\dot{x}^\alpha = -\frac{p^\alpha u_\alpha}{m^2} \left(p^\alpha + \frac{1}{2} \frac{S^{\alpha\beta} R_{\gamma\beta\mu\nu} p^\gamma S^{\mu\nu}}{m^2 + R_{\mu\nu\rho\sigma} S^{\mu\nu} S^{\rho\sigma} / 4} \right), \quad (11a)$$

$$\dot{p}^\alpha = -\Gamma^\alpha{}_{\mu\nu} p^\mu u^\nu + \frac{1}{2m} R^\alpha{}_{\beta\rho\sigma} \varepsilon^{\rho\sigma}{}_{\mu\nu} S^\mu p^\nu u^\beta, \quad (11b)$$

$$\dot{S}^\alpha = -\Gamma^\alpha{}_{\mu\nu} S^\mu u^\nu + \left(\frac{1}{2m^3} R_{\gamma\beta\rho\sigma} \varepsilon^{\rho\sigma}{}_{\mu\nu} S^\mu p^\nu S^\gamma u^\beta \right) p^\alpha. \quad (11c)$$

Here, the spin tensor $S^{\alpha\beta}$ in Eq. (11a) is understood as the expression (8). Eqs. (11) together with the constraint (10) constitute a closed system that we shall solve in the hairy BH background (2).

C. Initial Conditions

To numerically integrate the MPD equations, we must specify the initial conditions for the momentum p^α and the spin vector S^α . Since the BH is much more massive than the test particle, the particle's spin produces only a small correction to its geodesic motion, we

therefore construct the initial 4-momentum by first neglecting the spin, i.e., by solving the Hamilton-Jacobi equation for a spinless particle [51]:

$$g^{\mu\nu} \frac{\partial W}{\partial x^\mu} \frac{\partial W}{\partial x^\nu} + m^2 = 0, \quad (12)$$

where W is the Jacobi action, $p_\mu \equiv \partial W / \partial x^\mu$ is the canonical momentum.

The spherical symmetry of the background spacetime admits two Killing vectors, ∂_t and ∂_ϕ , yielding the conserved energy $E = -p_t$ and the axial angular momentum $L_z = p_\phi$. A third constant of motion, the Carter constant C , is introduced to separate the radial and polar motions. The Jacobi action can therefore be written in the separated form

$$W = -Et + \int \frac{\sqrt{R(r)}}{r^2 f(r)} dr + \int \sqrt{\Theta(\theta)} d\theta + L_z \phi, \quad (13)$$

with the functions $R(r)$ and $\Theta(\theta)$ given by

$$R(r) = r^4 E^2 - r^2 f(r) (r^2 + L_z^2 + C), \quad (14a)$$

$$\Theta(\theta) = C - \frac{L_z^2}{\sin^2 \theta} \cos^2 \theta. \quad (14b)$$

From the Hamilton-Jacobi formalism, the 4-velocities x^μ can be expressed by

$$\dot{x}^0 = \frac{E}{f(r)}, \quad (15a)$$

$$\dot{x}^1 = \frac{\sqrt{R(r)}}{r^2}, \quad (15b)$$

$$\dot{x}^2 = \frac{\sqrt{\Theta(\theta)}}{r^2}, \quad (15c)$$

$$\dot{x}^3 = \frac{L_z}{r^2 \sin^2 \theta}. \quad (15d)$$

The initial 4-momentum is then taken as

$$p^\mu = m \dot{x}^\mu. \quad (16)$$

This geodesic initial condition is an approximation. Once the spin is turned on, the actual evolution obeys the full MPD equations. Meanwhile, the directions of the 4-momentum and the 4-velocity are not parallel. Especially, E , L_z and C will no longer be strictly conserved. The validity of this approximation stems from the fact that worldlines induced by different SSCs deviate quite slightly (much smaller than the scale of the orbit), allowing the dynamics

to be dominated by the pole-dipole coupling rather than higher-order dipole-dipole terms. Consequently, the leading orders of 4-velocity and 4-momentum are parallel [51].

To facilitate the numerical integration of the equations of motion, we reformulate the conserved quantities in terms of orbital parameters [51, 52]. For generic bound orbits, we begin by relating the Carter constant C to the orbital inclination. In a Schwarzschild-like spacetime, the mapping can be written as

$$C = \frac{z_m^2 m^2 L_z^2}{1 - z_m^2}, \quad (17)$$

where $z_m \equiv \cos \theta_m$ and θ_m denotes the inclination angle. Substituting this expression into Eqs. (14) yields algebraic relations among the conserved energy E and the axial angular momentum L_z . We further introduce the standard Keplerian orbital parametrization, $r(X) = \frac{\mathcal{P}}{1+e \cos X}$, where \mathcal{P} is the semi-latus rectum and e is the eccentricity. Over one complete orbital period, the parameter X varies in the interval $[0, 2\pi]$. Within this parametrized framework, E and L_z can be expressed as functions of the orbital parameters $(\mathcal{P}, e, \theta_m)$. These relations will be employed in the following sections to construct particle trajectories. The detailed derivation is presented in Appendix A.

To complete the initial conditions, we further specify the spin vector. To this end, we work in the local orthonormal tetrad associated with spherical polar coordinates. A canonical choice for the tetrad components $\mathcal{S}_{\hat{\omega}}$ is

$$\mathcal{S}_{\hat{1}} = S \sin \tilde{\theta} \cos \tilde{\phi}, \quad (18a)$$

$$\mathcal{S}_{\hat{2}} = -S \cos \tilde{\theta}, \quad (18b)$$

$$\mathcal{S}_{\hat{3}} = S \sin \tilde{\theta} \sin \tilde{\phi}, \quad (18c)$$

$$\mathcal{S}_{\hat{0}} = 0, \quad (18d)$$

where S is the spin magnitude, and $\tilde{\theta}$, $\tilde{\phi}$ define its orientation. The condition $\mathcal{S}_{\hat{0}} = 0$ in Eq. (18d) is equivalent to enforcing the TD-SSC (10).

Since the particle moves in spherical spacetime, the spin vector in the global spherical frame should be [53]:

$$S^\mu = \mathcal{T}^\mu_{\hat{\omega}} \mathcal{S}^{\hat{\omega}}, \quad (19)$$

where $\mathcal{T}^\mu_{\hat{\omega}}$ is the spherical tetrad frame, due to the high symmetry of a spherical spacetime,

it takes a simple form:

$$\mathcal{T}^{\mu}_{\hat{0}} = (\sqrt{-g^{00}}, 0, 0, 0), \quad (20a)$$

$$\mathcal{T}^{\mu}_{\hat{1}} = (0, \sqrt{g^{11}}, 0, 0), \quad (20b)$$

$$\mathcal{T}^{\mu}_{\hat{2}} = (0, 0, \sqrt{g^{22}}, 0), \quad (20c)$$

$$\mathcal{T}^{\mu}_{\hat{3}} = (0, 0, 0, \sqrt{g^{33}}). \quad (20d)$$

Hence, the initial condition for the spin vector S^μ is obtained:

$$S^1 = S \sin \tilde{\theta} \cos \tilde{\phi} \sqrt{f(r)}, \quad (21a)$$

$$S^2 = -S \cos \tilde{\theta} / r, \quad (21b)$$

$$S^3 = S \sin \tilde{\theta} \sin \tilde{\phi} / (r \sin \theta), \quad (21c)$$

$$S^0 = -(p_1 S^1 + p_2 S^2 + p_3 S^3) / p_0. \quad (21d)$$

D. Orbital Dynamics

This subsection investigates the orbital dynamics of particles across hairy parameters $h = 0, 0.5$ and 1 ¹. The initial eccentricity is fixed at 0.75, with initial conditions $\theta = \frac{\pi}{2}$ and $\dot{\theta} = 0$.

To provide a baseline for comparison, we first analyze the orbital dynamics of a spinless particle ($S = 0$). It is important to note that one cannot obtain these orbits by simply setting $S = 0$ in the MPD equations. Theoretically, the motion of such a particle is governed by timelike geodesics, not the MPD system. Consequently, the data for the $S = 0$ scenario are computed from direct geodesic integrations.

Fig. 1 shows the orbital evolution of a spinless particle for increasing values of the hairy parameter: $h = 0, 0.5$, and 1 (from left to right). For $h = 0$ (left panel), the trajectory displays a prominent helical precession. The motion is predominantly confined to the x - y plane [54]. This helical geometry arises from the interplay between periodic angular motion and the same maximal radial distance. As the hairy parameter increases, the trajectory exhibits tighter precession pattern.

¹ We restrict our analysis to $h \geq 0$, since negative values induce pronounced orbital instability: even for modest $|h|$, the particle is scattered after only a few revolutions.

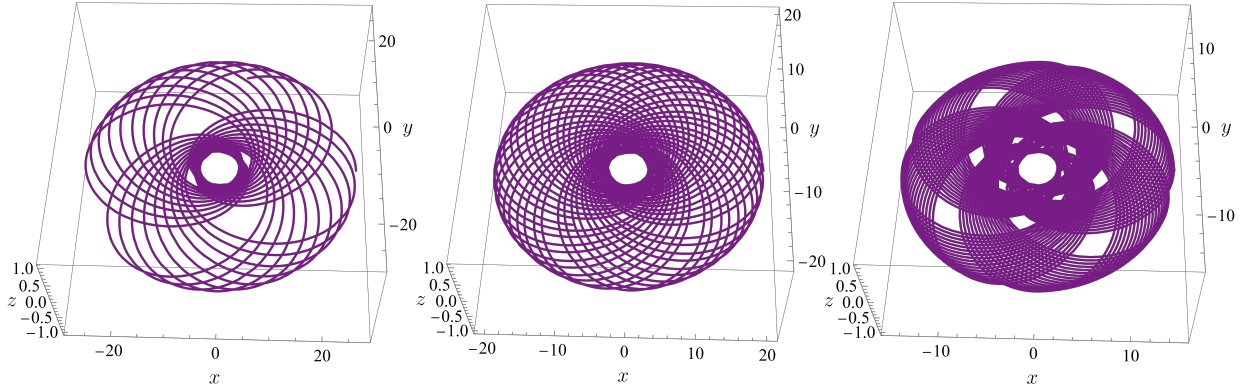


FIG. 1: Orbital evolution of a spinless particle for hairy parameter values $h = 0, 0.5,$ and 1 (left to right).

We next analyze the spinning particle case, which is governed by the MPD equations. Fig. 2 shows the corresponding orbital evolution for $S = 0.5$. In contrast to the spinless scenario, the spinning particle clearly deviates from equatorial motion. Specifically, spin induces a noticeable extension of the orbit along the z -axis. As h increases, the orbital evolution becomes more complex. Similar to the spinless case, the precession frequency rises with h . However, unlike the spinless trajectories, the x - y projection for $h = 0$ exhibits a distinct petal-like structure. This geometry originates from the periodic variation of the maximal orbital radius in each precession cycle. As h increases, the petal-like structure gradually fades.

Increasing the spin to its allowed maximum $S = 1$ (Fig. 3) leads to a further deviation from the equatorial plane. As with $S = 0.5$, the petal-like structure, clearly visible at $h = 0$, fades with increasing h . This fading behavior suggests a universal damping effect of scalar hair on the petal-like structure. Furthermore, scalar hair consistently increases the precession frequency, as also seen for $S = 0.5$.

To quantify the deviation from the equatorial plane evident in the orbital evolution, we define the measure

$$\tilde{r} = r \sin \theta - r, \quad (22)$$

with r being the spherical radial coordinate, thus $r \sin \theta$ represents the projected radius in the x - y plane. Here, a value of $\tilde{r} = 0$ indicates confinement to the equatorial plane.

Fig. 4 displays the evolution of \tilde{r} together with the polar angle θ for $S = 1$. It is important to note that the variable \tilde{t} used here and hereafter does not represent the true dynamical

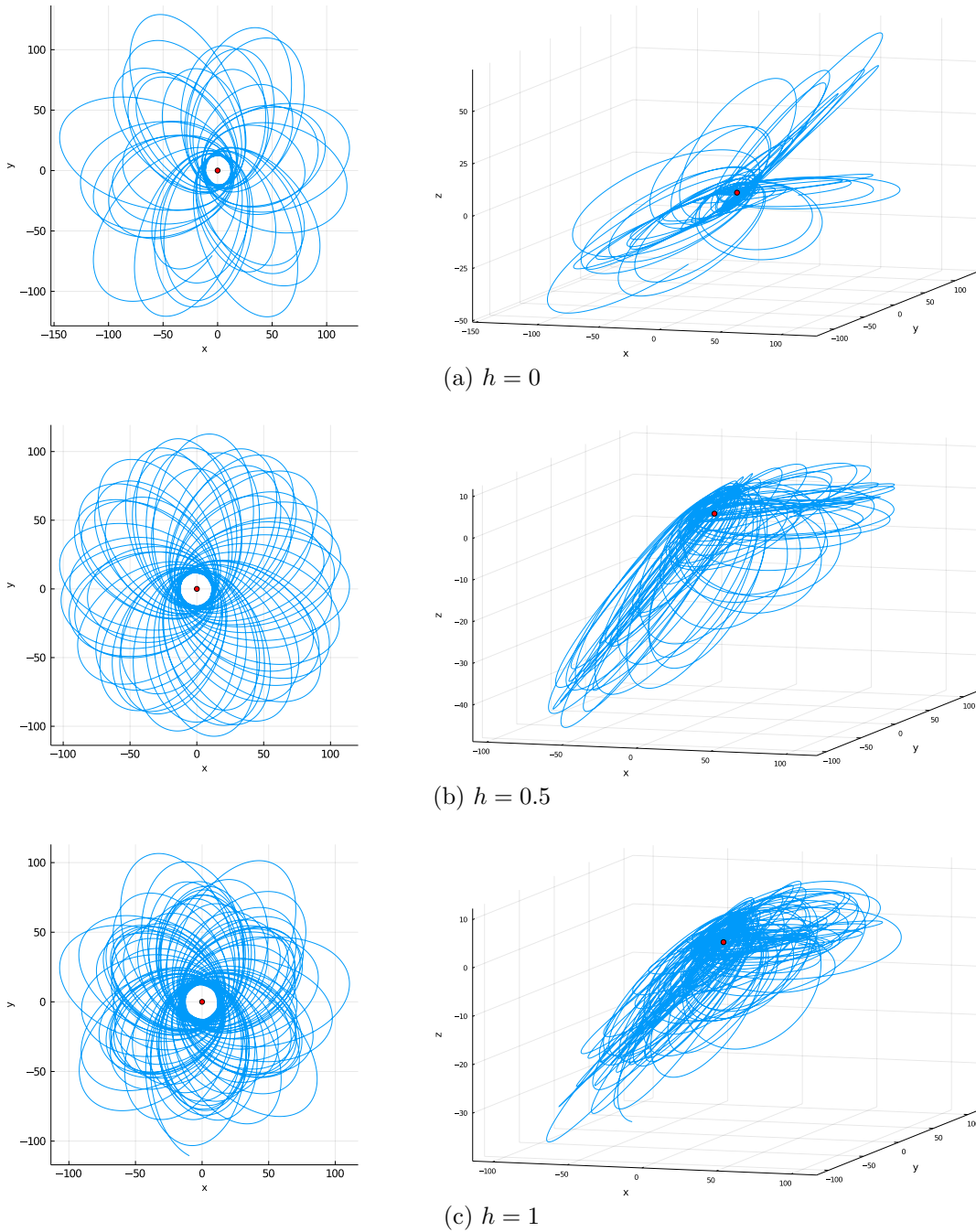


FIG. 2: Orbital evolution of a spinning particle ($S = 0.5$) for $h = 0, 0.5, 1$ (top to bottom). Left column: x - y projections. Right column: full three-dimensional trajectories.

time of the system, but merely denotes the sampling points. The proper time τ and the coordinate time t for this system will be introduced in Sec. V.

A key observation from Fig. 4 is the quasi-periodic oscillation of both \tilde{r} and θ , which shows clear synchronization with the orbital precession in Fig. 3. Increasing h suppresses

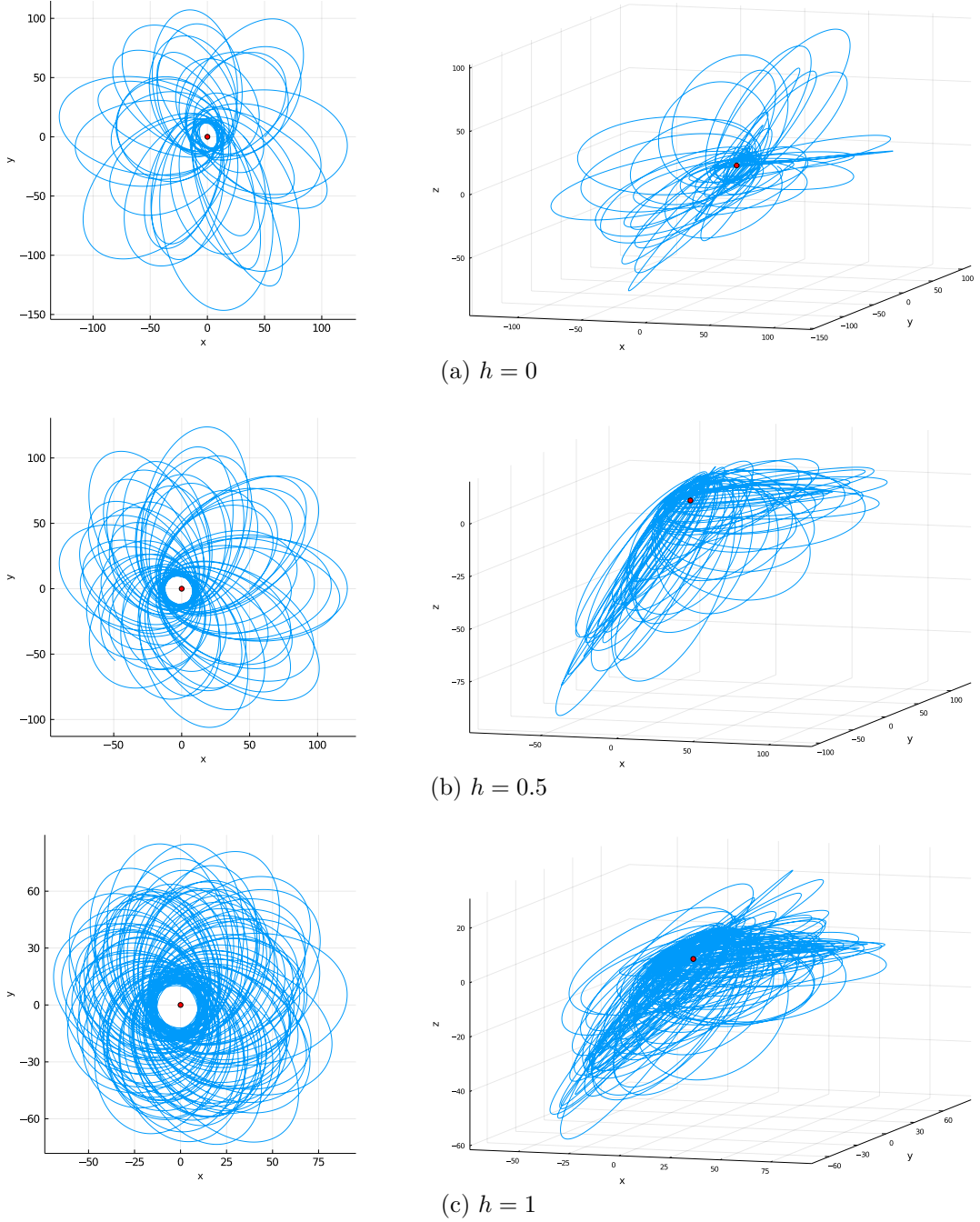


FIG. 3: Orbital evolution of a spinning particle ($S = 1$) for $h = 0, 0.5, 1$ (top to bottom). Left column: x - y projections. Right column: full three-dimensional trajectories.

the oscillation amplitudes of both \tilde{r} and θ and raises their frequencies. A direct consequence is the reduction in the peak-to-peak range of \tilde{r} . Therefore, as h grows, the cyclic change in the maximal precession distance becomes less pronounced, indicating that the orbit evolves towards a more regular precession pattern. This quantitative result is consistent with the

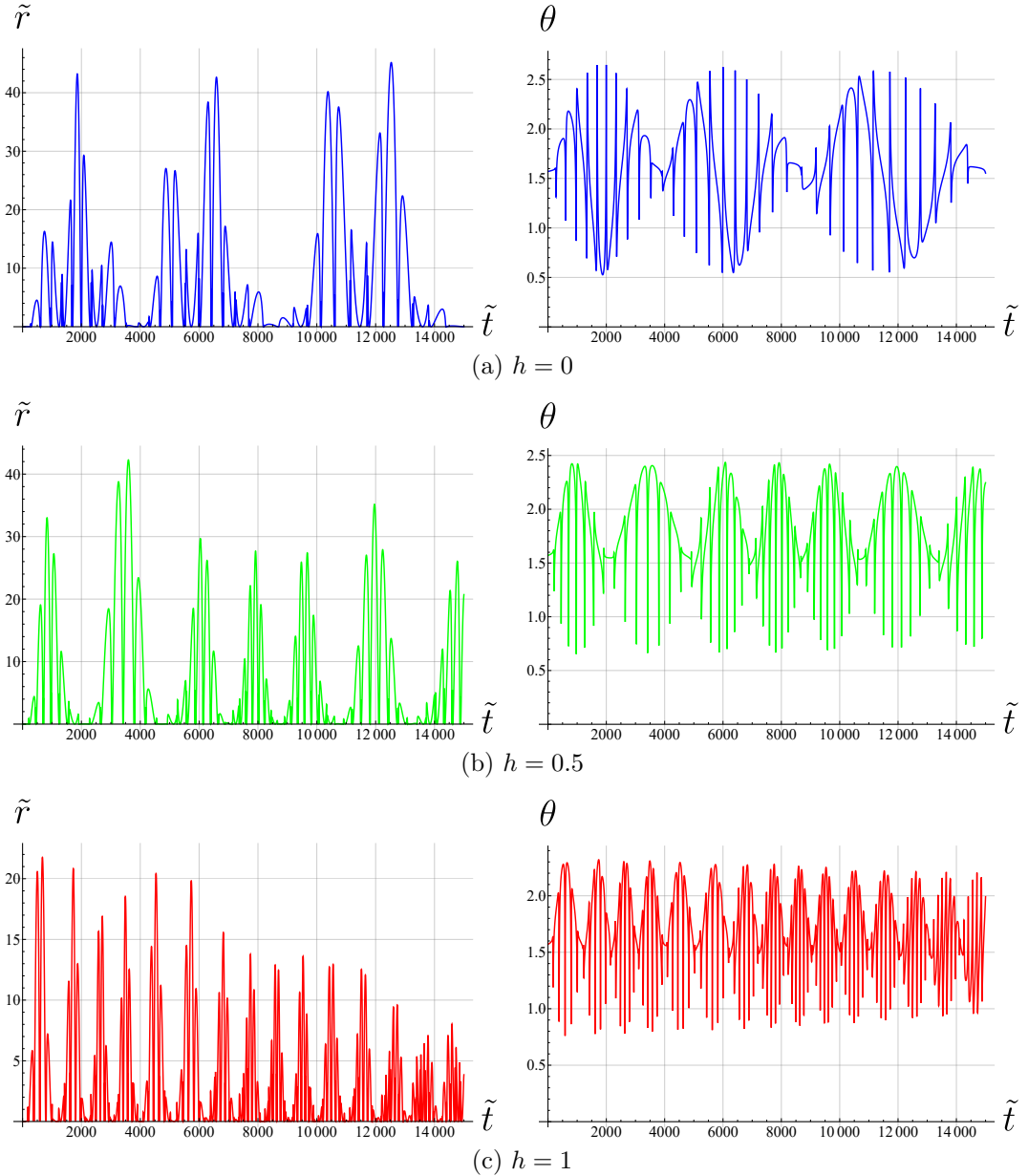


FIG. 4: Shown are \tilde{r} (left) and the polar angle θ (right) as functions of the sampling index \tilde{t} , for $S = 1$.

orbital evolution observed in Fig. 3.

III. EFFECTIVE POTENTIAL ANALYSIS

To illustrate the explicit effect of spin, we examine the effective potential of a spinning test particle in the Horndeski hairy BH spacetime.

A. Effective Potential

Our first step is to derive analytic expressions for each component of the spin tensor. This task is tractable because of the spacetime's spherical symmetry. For a spinning particle, a conserved quantity Y along its worldline can be constructed from the Killing vector ξ^μ of the background [11]. It is defined as

$$Y = \xi^\mu p_\mu - \frac{1}{2} \xi_{\mu;\nu} S^{\mu\nu}, \quad (23)$$

where the semicolon denotes covariant differentiation.

Using the Killing vectors associated with the static and axial symmetries, $\xi_{(t)}^\mu = (1, 0, 0, 0)$ and $\xi_{(\phi)}^\mu = (0, 0, 0, 1)$, we obtain two constants of motion:

$$E = -Y_{(0)} = -p_0 - \frac{1}{2} f'(r) S^{01}, \quad (24a)$$

$$L_z = Y_{(3)} = p_3 + r(rS^{23} \cos \theta \sin \theta + S^{13} \sin^2 \theta). \quad (24b)$$

The spherical symmetry also guarantees conservation of the remaining Cartesian components of angular momentum, with the corresponding Killing vectors given by

$$\xi_{(x)}^\mu = (0, 0, -\sin \phi, -\cot \theta \sin \phi), \quad \xi_{(y)}^\mu = (0, 0, \cos \phi, -\cot \theta \sin \phi). \quad (25)$$

Inserting Eq. (25) into Eq. (23), we have

$$L_x = -p_2 \sin \phi - p_3 \cot \theta \cos \phi + r^2 S^{23} \sin^2 \theta \sin \phi - r S^{13} \sin \theta \cos \theta \sin \phi + r S^{12} \cos \phi, \quad (26a)$$

$$L_y = p_2 \cos \phi - p_3 \cot \theta \sin \phi + r^2 S^{23} \sin^2 \theta \cos \phi - r S^{13} \sin \theta \cos \theta \cos \phi + r S^{12} \sin \phi. \quad (26b)$$

Without loss of generality we align the total angular momentum with the z -axis, i.e. we set $(L_x, L_y, L_z) = (0, 0, L)$. This choice yields the following solutions for the spatial components of the spin tensor:

$$S^{12} = -\frac{p_2}{r}, \quad (27a)$$

$$S^{13} = \frac{1}{r} \left(L - \frac{p_3}{\sin^2 \theta} \right), \quad (27b)$$

$$S^{23} = \frac{L \cot \theta}{r^2}. \quad (27c)$$

The remaining components S^{0i} are determined from the TD-SSC (4). Substituting the above

results gives

$$S^{01} = -\frac{1}{rp_0} \left[(p_2)^2 + \frac{(p_3)^2}{\sin^2 \theta} - Lp_3 \right], \quad (28a)$$

$$S^{02} = \frac{1}{rp_0} \left(p_1 p_2 + \frac{Lp_3}{r} \cot \theta \right), \quad (28b)$$

$$S^{03} = -\frac{1}{rp_0} \left(Lp_1 - \frac{p_1 p_3}{\sin^2 \theta} + \frac{Lp_2}{r} \cot \theta \right). \quad (28c)$$

Inserting the expression for S^{01} into the conserved energy equation (24a) leads to a compact formula as follows:

$$E = -p_0 + \frac{(p_2)^2 - Lp_3 + (p_3)^2 \csc^2 \theta}{2p_0 r} f'(r). \quad (29)$$

Finally, we restrict the spin to lie in the meridian plane [11], which implies $p^1 = 0$ and $p^2 = 0$. Under this assumption, we parameterize the remaining momentum components as

$$p_0 = -m f^{1/2}(r) \cosh X(r, \theta), \quad (30a)$$

$$p_3 = mr \sin \theta \sinh X(r, \theta), \quad (30b)$$

where $X(r, \theta)$ is a function to be determined. Substituting Eqs. (30) into the spin tensor solutions obtained above yields the following forms

$$S^{01} = -\frac{1}{\sqrt{f(r)}} [-L \sin \theta + mr \sinh X(r, \theta)], \quad (31a)$$

$$S^{02} = -\frac{L \cos \theta}{r \sqrt{f(r)}} \tanh X(r, \theta), \quad (31b)$$

$$S^{03} = 0, \quad (31c)$$

$$S^{12} = 0, \quad (31d)$$

$$S^{13} = \frac{L}{r} - m \csc \theta \sinh X(r, \theta), \quad (31e)$$

$$S^{23} = \frac{L \cot \theta}{r^2}. \quad (31f)$$

To determine $\sinh X(r, \theta)$, we first insert the given spin tensor into Eq. (9), yielding the expanded form:

$$S^2 = \frac{1}{2} S_{\mu\nu} S^{\mu\nu} = -S_{01}^2 + \frac{r^2 S_{12}^2}{f(r)} - r^2 S_{02}^2 f(r) + r^4 S_{23}^2 \sin^2 \theta + \frac{r^2 S_{13}^2 \sin^2 \theta}{f(r)} - r^2 S_{03}^2 f(r) \sin^2 \theta. \quad (32)$$

Using Eqs. (31), the conserved spin relation can be recast as:

$$-S^2 f(r) + [L^2 \cos^2 \theta f(r) + (L \sin \theta + mr \sinh X(r, \theta))^2] / \cosh^2 X(r, \theta) = 0, \quad (33)$$

and $\sinh X(r, \theta)$ is then directly obtained:

$$\sinh X(r, \theta) = \frac{\omega(r, \theta) \pm \sqrt{\omega^2(r, \theta) - \varsigma(r)[(L^2 - S^2)f(r) + L^2 \sin^2 \theta(1 - f(r))]}{\varsigma(r)}, \quad (34a)$$

$$\omega(r, \theta) = mr \sin \theta \sinh X(r, \theta), \quad (34b)$$

$$\varsigma(r, \theta) = m^2 r^2 - S^2 f(r). \quad (34c)$$

Since the possible trajectories of the particle are governed by its energy (Eq. (29)) and effective potential V with $V^2 \leq E^2$, we focus on the critical case:

$$E = V_{(\pm)}(r, \theta, L, S) = \frac{mf^{1/2}(r)\sqrt{1 + \sinh^2 X(r, \theta)} + [L \sin \theta - mr \sinh X(r, \theta)] \sinh X(r, \theta) f'(r)}{2\sqrt{f(r)[1 + \sinh X(r, \theta)]}}. \quad (35)$$

The sign \pm corresponds to the orientation of the particle's spin relative to the total angular momentum L : $V_{(-)}$ describes the configuration where the spin is parallel to L , while $V_{(+)}$ corresponds to the antiparallel case. In the following we adopt the parallel configuration, i.e., we work with $V_{(-)}$. The particle with potential $V_{(-)}$ can move more closer to the event horizon [11].

Following the classification of effective potentials in Ref. [11], there are four distinct types: restrictive (B1, B2) and non-restrictive types (U1, U2). Type (B1), characterized by large angular momentum L and relatively small spin S , exhibits no chaos. As the spin increases, the system switches to type (B2), where chaotic behavior emerges. Both non-restrictive types are associated with small L : type (U1) involves low spin, while type (U2) features higher spin; neither exhibits chaos. The four types and their key features are summarized in Table I.

Since chaotic motion is associated with the high-spin restrictive type (B2), we primarily focus on the case $S = 1$, which serves as the physically allowed upper spin limit and is expected to display strong chaotic behavior. In the following Sec. IV, we investigate how the Horndeski hair influences this chaotic dynamics.

B. Effective Potential Metaphor and Saddle Points

In this subsection, we analyze the effective potential in cylindrical coordinates (ρ, z) (see Fig. 5) to elucidate the orbital dynamics from the preceding subsection and the ensuing

Category	Potential Type	Angular Momentum (L)	Spin (S)	Key Features
B1	Restrictive	Large	Low	No chaos
B2	Restrictive	Large	Higher ($> B1$)	chaos
U1	Non-restrictive	Small	Low	No chaos
U2	Non-restrictive	Small	Higher ($> U1$)	No chaos

TABLE I: Classification of the effective potentials.

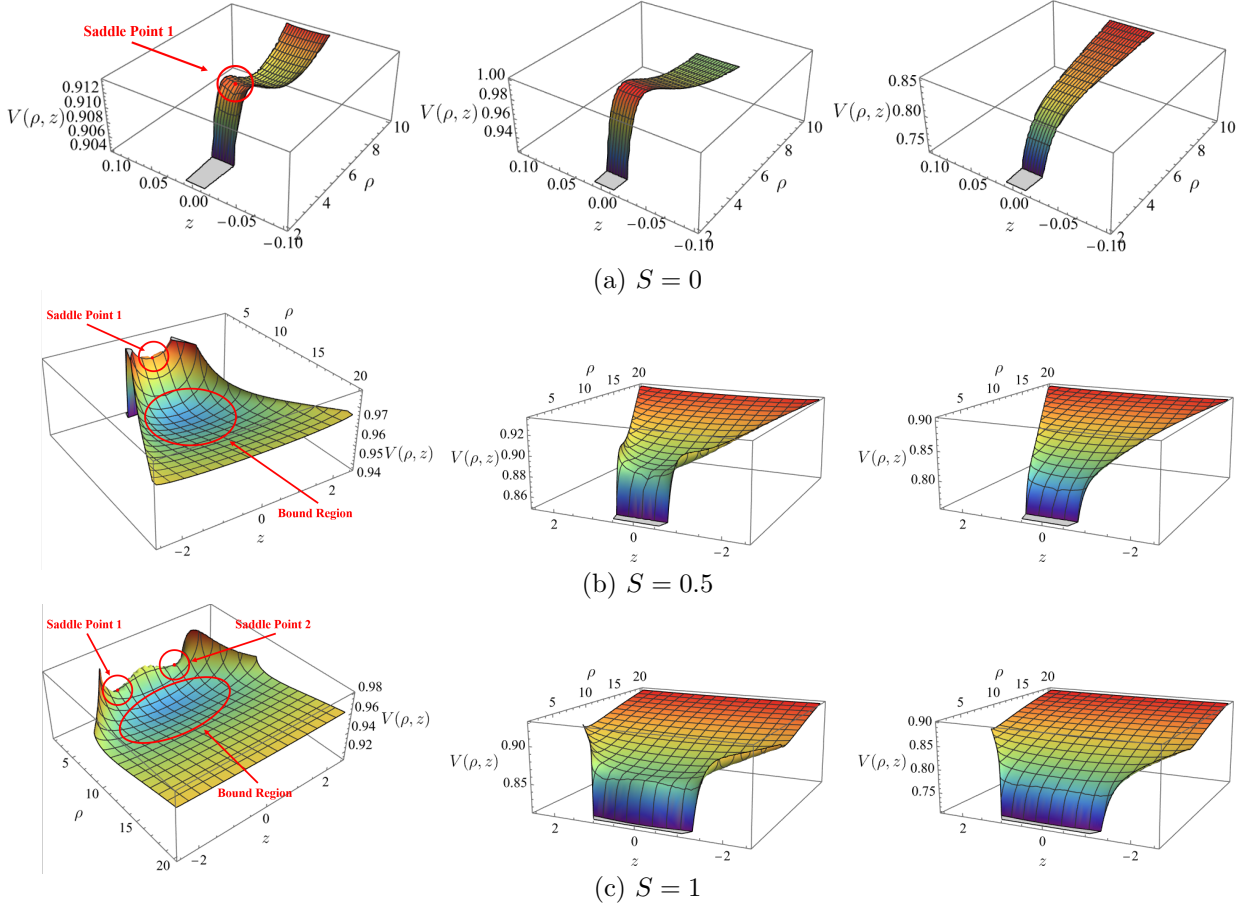


FIG. 5: Effective potentials in cylindrical coordinates, varying over the hairy parameter h (columns: 0, 0.5, 1) and the particle spin S (rows: 0, 0.5, 1).

chaotic behavior. Our discussion is organized by the particle spin S , with each value (0, 0.5, 1) illustrating a key stage in the transition to chaos, and examines the impact of the hairy parameter h (0, 0.5, 1). The key properties of the potential are summarized below.

- **No scalar hair ($h = 0$).**

- **Spinless case** ($S = 0$). The potential is sharply confined near $z = 0$ and attains its extremum on the equatorial plane ($z = 0$), forming a single saddle point that confines the particle motion. This structure, characteristic of a type (B1) potential, explains the planar orbits observed in Fig. 1.
 - **Low-spin case** ($S = 0.5$). With spin, the potential extends its distribution and develops a barrier along the z -direction near the horizon, permitting off-plane motion. While a single saddle point on the equatorial plane maintains a bound region (still type (B1)), the z -barrier allows the particle to reach varying maximal distances in successive precession cycles by “sliding” from the barrier, leading to the petal-like x - y projection.
 - **Maximal-spin case** ($S = 1$). At maximal spin $S = 1$, the equatorial saddle point bifurcates into two, located symmetrically off the plane. This creates a new bound region, characteristic of a type (B2) potential, within which the particle executes complex retrograde motion — the direct source of the observed chaos.
- **Effect of the hairy parameter.** Increasing h flattens the potential, lowering barriers, erasing saddle points, and ultimately destroying the bound regions. This reduces the variation in maximal precession distance, explaining the fading of the petal-like orbits in Figs. 2 and 3. The system is notably sensitive for $S = 1$, with saddle points vanishing at $h_{\text{crit}} = 0.2805$. For large h , the potential becomes monotonic, resembling a non-restrictive type (U) where no chaos occurs.

IV. CHAOTIC DYNAMICS ANALYSIS

A key signature of chaotic dynamics is a positive LE λ , which quantifies the average rate of divergence between nearby trajectories. When the numerically computed maximal LE converges to a positive value, it reliably indicates the presence of chaos in the system. Meanwhile, in the procedure of calculating the LE, we will rebuild the Lorenz attractor, which is a set encompassing all possibly dynamical states of a particle in long-time evolution.

Another crucial indicator of chaos is the Poincaré section, a lower-dimensional projection of the phase space. Chaotic motion is characterized by a scatter of discrete points on the Poincaré section, in contrast to the smooth, closed curve produced by regular motion. This

occurs because the trajectory, due to its chaotic nature, never returns exactly to a previous point after one period, and each intersection with the section lands at a distinct location. Over sufficient time, these points can form intricate fractal structures (see Appendix B).

In this section, we investigate how the scalar hair parameter h influences these chaotic indicators with the situation $S = 1$. To this end, we first reconstruct the phase space of the system via Takens' embedding theory in subsection IV A. We then introduce the Wolf algorithm for computing LEs in subsection IV B. In subsection IV C, we numerically calculate these chaotic indicators and analyze the chaotic properties of the system.

A. Takens' Embedding Theory

Having obtained the numerical data by integrating the MPD equations, we can reconstruct the phase space of the system using Takens' embedding theorem [55]. According to Takens' theory, a time series of a single dynamical variable contains sufficient information to reconstruct a new phase space that is diffeomorphic to the original one [56]. Let the true (unknown) state of the dynamical system be represented by a vector in the original phase space

$$\mathbf{A}(t) = (\alpha_1(t), \alpha_2(t), \dots, \alpha_{\mathcal{D}}(t)), \quad (36)$$

where \mathcal{D} is the dimension of the original phase space. Suppose we measure a scalar observable

$$s(t) = \mathcal{M}(\alpha_1(t)), \quad (37)$$

where \mathcal{M} is a smooth measurement function. According to Takens' embedding theorem, a topologically equivalent phase space can be reconstructed from the time series $s(t)$ via delay coordinates

$$\mathbf{B}(t) = (s(t), s(t+T), s(t+2T), \dots, s(t+(c-1)T)). \quad (38)$$

Here, T is the time delay, chosen as an integer multiple of the sampling interval Δt . The embedding dimension c must satisfy $c > 2D$, D is the dimension of the original Lorenz attractor. The mapping $\Phi : \mathbf{A}(t) \rightarrow \mathbf{B}(t)$ is then an embedding. Φ and its inverse Φ^{-1} are smooth one-on-one mappings and diffeomorphisms, preserving invariant quantities such as Lorenz attractor and LEs.

A useful analogy is viewing a three-dimensional object under varying illumination: its one-dimensional shadow changes with the light direction. Takens' theorem guarantees that if

we record the shadow from sufficiently many independent viewpoints, namely an adequate embedding dimension c , the full object can be uniquely reconstructed. In practice, one should choose an observable that best reflects the irregular, chaotic nature of the dynamics. Here we use the radial coordinate $r(t)$ as the measured variable. Other scalar functions that depend nonlinearly on the state, e.g., kinetic or potential energy, could also serve as suitable observables.

B. Wolf Algorithm for LEs

To compute the LEs numerically we employ the Wolf algorithm [57]. Based on the new phase space (38), the Wolf algorithm can numerically implement the definition of LE. Its main idea is to trace a long-time evolution of elements in an infinite small bulk. Our goal is to approach the maximal LE:

$$\lambda_{max} = \lim_{t \rightarrow \infty} \lim_{|\delta \mathbf{Z}(0)| \rightarrow 0} \frac{1}{t} \log_2 \frac{|\delta \mathbf{Z}(t)|}{|\delta \mathbf{Z}(0)|}, \quad (39)$$

where $\delta \mathbf{Z}(t)$ is the deviate vector between two points in the phase space at time t .

The procedure begins by choosing an initial point $\Omega(t_0)$ from Eq. (38) on a fiducial trajectory. Within a small sphere of radius d centered at this point, we then locate its closest neighbour, denoted $\Omega(t_0')$. Then we have an initial separation $L_0 = \|\Omega(t_0) - \Omega(t_0')\| < d$. The appropriate value of the search radius d depends on the purity of the data: cleaner data (high signal-to-noise ratio) support a smaller d . In our study, the data come from the numerical solution of equations of motion, which are inherently noiseless. We therefore set d to a small value to ensure the precision of the LE computation.

In the second step, the two points $(\Omega(t_0), \Omega(t_0'))$ evolve in steps k along their trajectories. The evolved points are $(\Omega(t_0 + k), \Omega(t_0' + k))$, and the distance between them becomes $L_0' = \|\Omega(t_0 + k) - \Omega(t_0' + k)\|$. This evolution, which leads to an increase in the exponent, is quantified by the following relation:

$$\Delta \lambda = \frac{1}{k \cdot \Delta t} \log_2 \frac{|\delta \mathbf{Z}(t)|}{|\delta \mathbf{Z}(0)|}, \quad (40)$$

where the prefactor $\frac{1}{k \cdot \Delta t}$ serves as a normalization constant.

After evolution, the separation L_0' is compared with the prescribed radius d . If $L_0' \leq d$, the evolved pair is retained and the procedure proceeds to the next segment. If $L_0' > d$, a

replacement neighbour must be chosen. We select a new point $\Omega(t_1')$ in the neighbour of the current fiducial point $\Omega(t_0 + k)$ such that the new separation

$$L_1 = \|\Omega(t_0 + k) - \Omega(t_1')\|, \quad (41)$$

satisfies $L_1 < d$. Furthermore, the direction of the new vector $\Omega(t_0 + k)\Omega(t_1')$ should be as close as possible to the old one $\Omega(t_0 + k)\Omega(t_0' + k)$. This process is equivalent to perform a Gram-Schmidt reorthonormalization in the tangent space of a continuous dynamical system. It ensures that we are tracing the most unstable direction, the one associated with the maximal LE. Finally, we repeat the second and third steps until the whole time series is traversed. The maximal LE is the time average of these local increasing rates:

$$\lambda_{max} \approx \frac{1}{K} \sum_{i=1}^K \frac{1}{k_i \cdot \Delta t} \log_2 \frac{L_i'}{L_i}, \quad (42)$$

where K is the total number of segments (evolution-renormalization cycles) processed.

C. Indicators of Chaotic Dynamics

To characterize the stability of a dynamical system, we examine three complementary diagnostics: Poincaré sections, Lorenz attractors, and the maximal LE. These results are presented for varying hair parameter h , with the Lorenz attractors and Poincaré sections shown in the left and right columns of Fig. 6, respectively, and the maximal LE shown in Fig. 7.

In the rebuilt Lorenz attractor, the interpretation of the coordinate axes depends on the variable selected for phase space reconstruction. In this work, we use the radial coordinate; accordingly, all axes correspond to the same variable, but at successively delayed times. Specifically, the x -axis represents the current value $r(\tau)$, while the y - and z -axes correspond to the delayed values $r(\tau - \Delta\tau)$ and $r(\tau - 2\Delta\tau)$, respectively.

Fig. 6 shows that the Lorenz attractor for $h = 0$ is sharper and more elongated than those for $h = 0.5$ and $h = 1$, occupying a larger region in phase space. This indicates that, over the same proper-time interval, the particle traverses a greater distance. Therefore, two initially nearby trajectories are separated at a higher rate, reflecting a stronger orbital instability. As Horndeski hair h increases, the attractor becomes smoother and more confined to a smaller region. Consistent with this contraction, the maximum radial excursion in each

precession cycle decreases progressively for $h = 0.5$ and $h = 1$ in Fig. 4, implying a slower rate of divergence between neighboring orbits. A parallel trend appears in the Poincaré sections: the scattered points are gradually compressed into a smaller domain as h grows. The maximal values of r in the left and right columns of Fig. 6 correspond one to one, confirming the consistency between the two diagnostic methods. On the other hand, the maximal LE quantifies the degree of chaos in the system. The calculated LEs decrease with increasing h , as shown in Fig. 7. This decline supports the conclusion that a growing Horndeski hair suppresses the chaotic motion of a spinning particle orbiting the BH.

As discussed in Sec. III, although increasing h removes the saddle points along the z -axis, chaotic motion persists here. This phenomenon can be attributed to the relatively large initial distance of the particle, and the scale of the motion on r -axis is much wider than the potential distribution on z -axis. Meanwhile, motion in the θ -direction is constrained by the conserved angular momentum, so that its dynamics are confined to a low-dimensional submanifold of phase space, making the θ -sector integrable. This mechanism greatly weakens the coupling between r and θ . Consequently, as seen in Fig. 4, θ exhibits quasi-periodic oscillation rather than exponential divergence, confining the chaotic dynamics primarily to the radial direction.

V. GRAVITATIONAL WAVEFORM

To assess whether the hairy parameter has a practically observable effect on chaotic motion, we analyze the GW signals generated by the quadrupole moment in subsections VA and VB, focusing on the degree of match between its two polarization modes. In subsection VC, we perform the corresponding time conversion for actual observations and provide a discussion.

A. Quadrupole Formula

To compute the gravitational waveform emitted by the spinning particle, we adopt the quadrupole formula, a well-established approximation valid for distant observers when the observer's distance r_{obs} greatly exceeds the orbital scale. This approach requires constructing the metric perturbation in the transverse-traceless (TT) gauge [58–60]. Below, we detail the

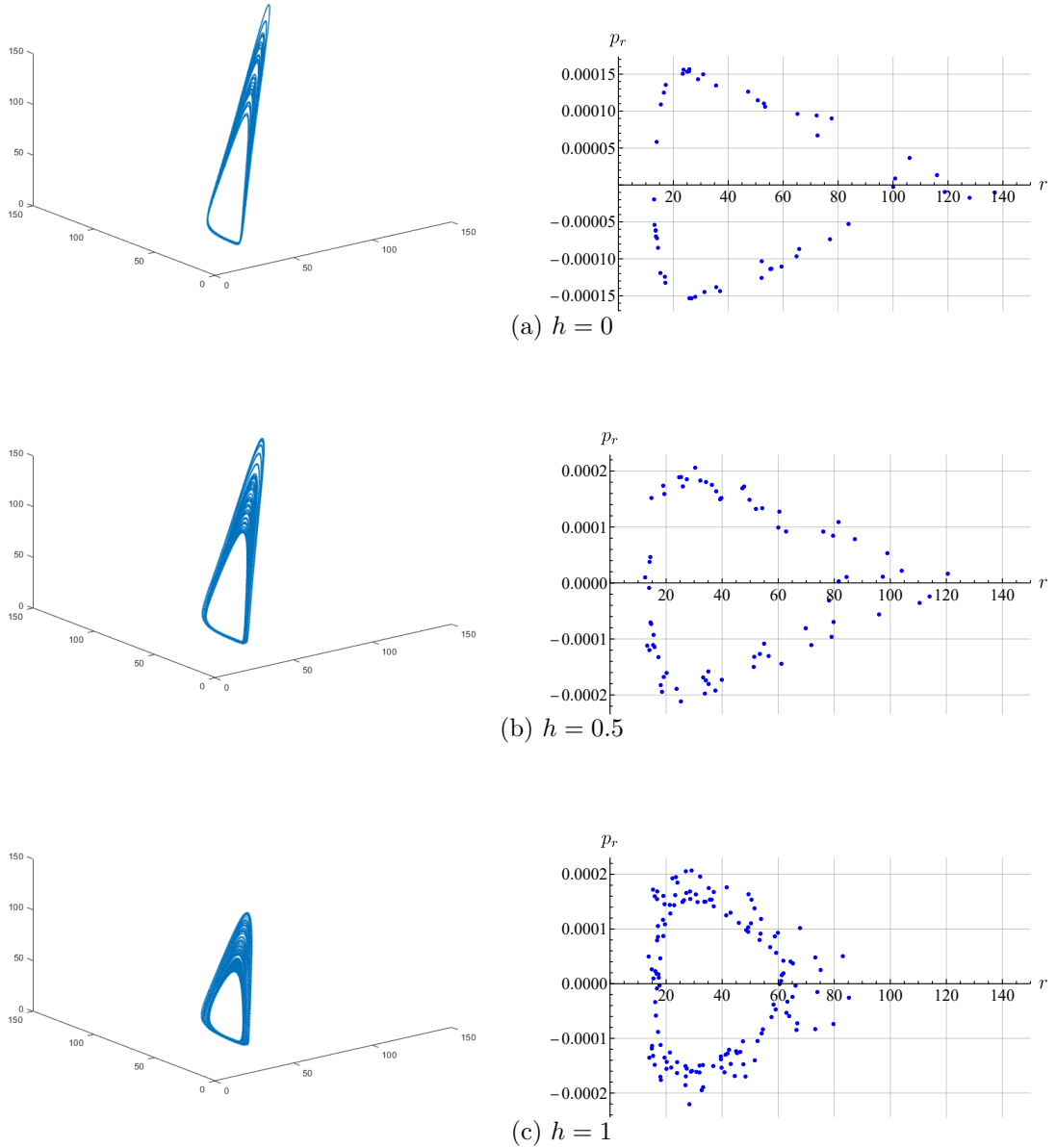


FIG. 6: Lorenz attractors (left column) and Poincaré sections (right column) for a spin parameter of $S = 1$.

key steps for calculating the two independent polarization modes h_+ and h_\times of the GW, starting from the definition of the TT gauge and the mass-quadrupole moment.

We first set up an orthonormal triad aligned with the observer's direction:

$$\mathbf{n} = (\sin \theta_{obs} \cos \phi_{obs}, \sin \theta_{obs} \sin \phi_{obs}, \cos \theta_{obs}), \quad (43a)$$

$$\mathbf{m} = (\cos \theta_{obs} \cos \phi_{obs}, \cos \theta_{obs} \sin \phi_{obs}, -\sin \theta_{obs}), \quad (43b)$$

$$\mathbf{l} = (-\sin \phi_{obs}, \cos \phi_{obs}, 0), \quad (43c)$$

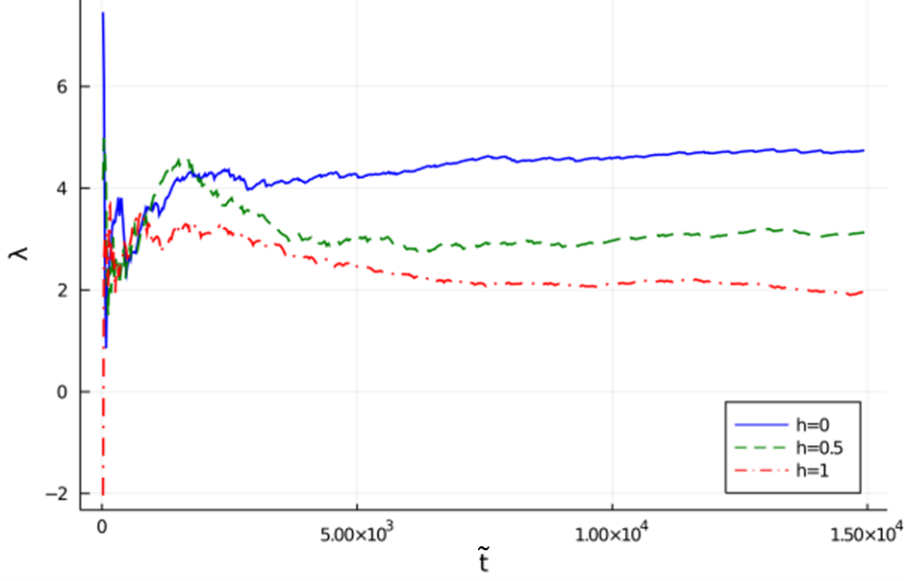


FIG. 7: LEs for various hairy parameters at $S = 1$.

where the unit vector \mathbf{n} points in the observer's direction, \mathbf{m} and \mathbf{l} form an orthogonal basis in the plane transverse to \mathbf{n} . Here, θ_{obs} and ϕ_{obs} denote the observer's polar and azimuthal angles, respectively. The corresponding “plus” and “cross” polarization tensors are then

$$(e_+)_{ij} = m_i m_j - l_i l_j, \quad (44a)$$

$$(e_\times)_{ij} = m_i l_j + l_i m_j. \quad (44b)$$

The second time-derivative of the mass-quadrupole moment in Cartesian coordinates is

$$\ddot{Q}_{ij} = m(\ddot{x}_i x_j + 2\dot{x}_i \dot{x}_j + x_i \ddot{x}_j), \quad (45)$$

where $x_i(t)$ are the coordinates obtained from integrating the MPD equations. To enforce the traceless condition we subtract the trace part of \ddot{Q}_{ij} :

$$\ddot{Q}_{ij}^{tf} = \ddot{Q}_{ij} - \frac{1}{3} \delta_{ij} \sum_k \ddot{Q}_{kk}. \quad (46)$$

Then we project the trace-free quadrupole moment with a TT projection operator:

$$\Lambda_{ij,kl} = P_{ik} P_{jl} - \frac{1}{2} P_{ij} P_{kl}, \quad (47)$$

where the transverse projection operator P_{ij} is given by

$$P_{ij} = \delta_{ij} - n_i n_j. \quad (48)$$

This leads to the expression for the metric perturbation:

$$h_{ij} = \frac{2}{r_{obs}} \Lambda_{ij,kl} \ddot{Q}_{kl}^{tf}. \quad (49)$$

The two independent polarization modes h_+ and h_\times are obtained by contracting h_{ij} the respective polarization tensors $(e_+)^{ij}$ and $(e_\times)^{ij}$, which yield:

$$\begin{aligned} h_+ &= h_{ij} (e_+)^{ij} \\ &= (h_{xx} - h_{yy}) \frac{(\cos^2 \theta_{obs} + 1)}{4} \cos 2\phi_{obs} \\ &\quad - \frac{(h_{xx} + h_{yy} - 2h_{zz})}{4} \sin^2 \theta_{obs} + h_{xy} \left(\frac{\cos^2 \theta_{obs} + 1}{2} \right) \sin 2\phi_{obs} \\ &\quad - h_{xz} \sin \theta_{obs} \cos \theta_{obs} \cos \phi_{obs} - h_{yz} \sin \theta_{obs} \cos \theta_{obs} \sin \phi_{obs}, \end{aligned} \quad (50a)$$

$$\begin{aligned} h_\times &= h_{ij} (e_\times)^{ij} \\ &= -\frac{(h_{xx} - h_{yy})}{2} \cos \theta_{obs} \sin 2\phi_{obs} + h_{xy} \cos \theta_{obs} \cos 2\phi_{obs} \\ &\quad + h_{xz} \sin \theta_{obs} \sin \phi_{obs} - h_{yz} \sin \theta_{obs} \cos \phi_{obs}. \end{aligned} \quad (50b)$$

In the following, we set the observer at the position $(r_{obs}, \theta_{obs}, \phi_{obs}) = (5000, \frac{\pi}{4}, 0)$.

B. Gravitational Waveform Signatures

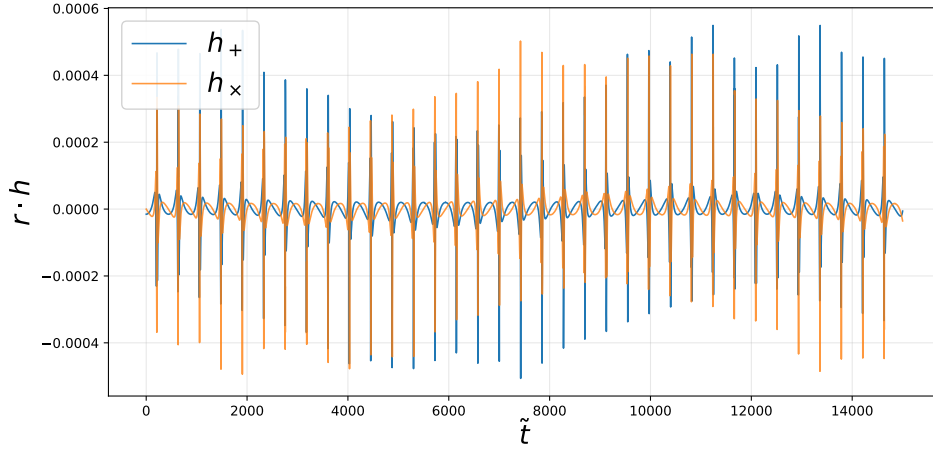
Before proceeding, we first introduce the key statistical metrics: the cross-correlation (CC) coefficient and the mean absolute error (MAE) between h_+ and h_\times [61] to quantify the evolving phase coherence. They are defined as

$$CC = \frac{\sum_{i=1}^n (h_+^i - \bar{h}_+) (h_\times^i - \bar{h}_\times)}{\sqrt{\sum_{i=1}^n (h_+^i - \bar{h}_+)^2 \sum_{i=1}^n (h_\times^i - \bar{h}_\times)^2}}, \quad (51a)$$

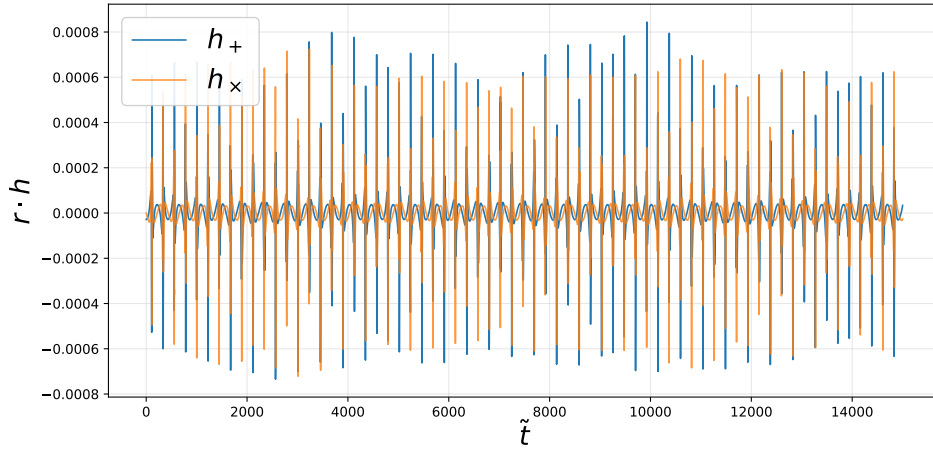
$$MAE = \frac{1}{n} \sum_{i=1}^n |h_+^i - h_\times^i|, \quad (51b)$$

where n is the total number of time samples, and \bar{h}_+ , \bar{h}_\times denote the mean values of the respective time series.

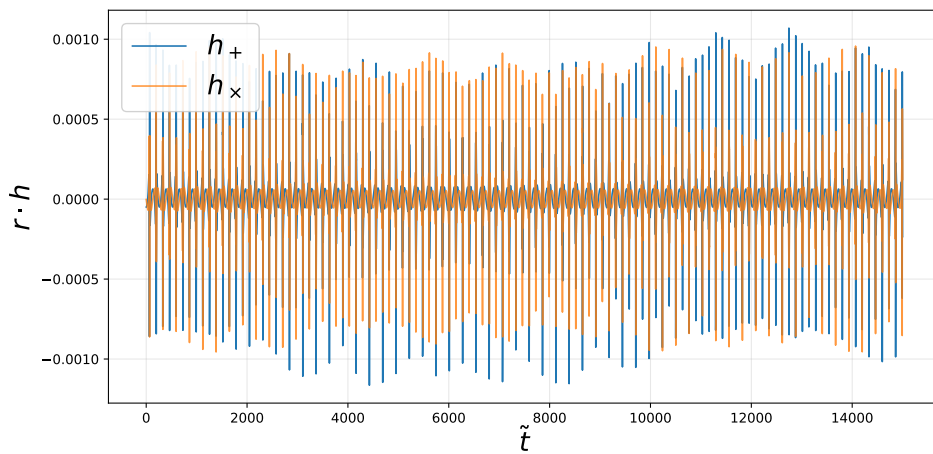
Building on the quadrupole formula derived in subsection V A, we analyze the gravitational waveforms emitted by the spinning particle, specifically the two independent polarization modes h_+ and h_\times , and quantify how scalar hair modulates their phase coherence. The



(a) $h = 0$

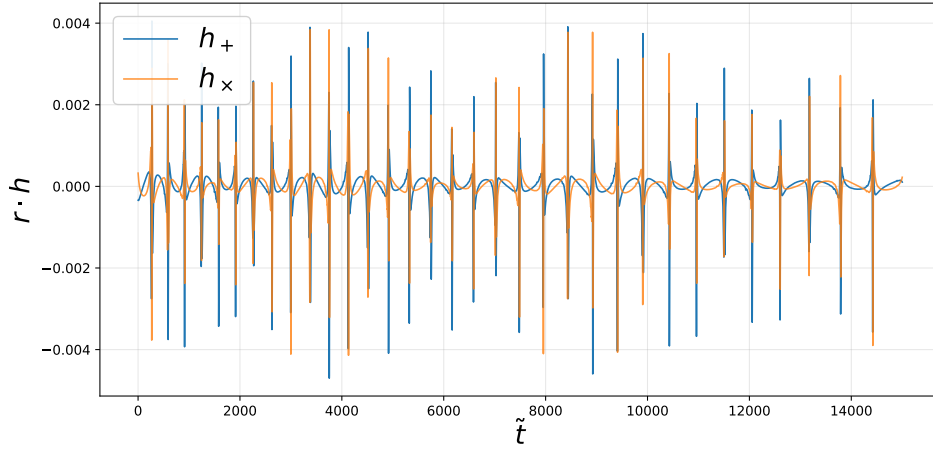


(b) $h = 0.5$

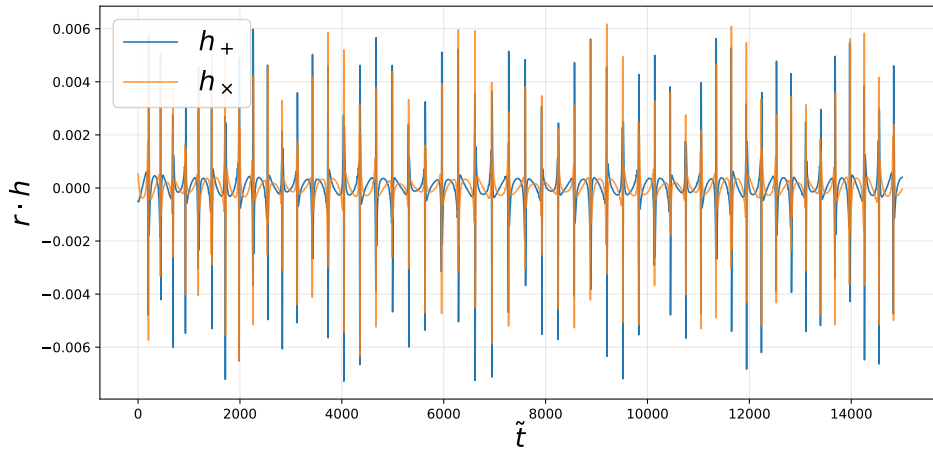


(c) $h = 1$

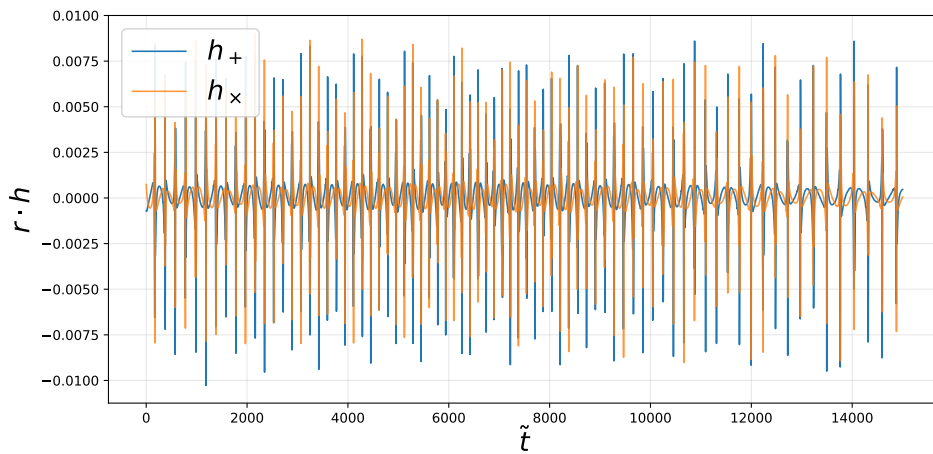
FIG. 8: Gravitational waveforms for $S = 0$. The blue and orange lines represent the plus polarization h_+ and the cross polarization h_\times , respectively.



(a) $h = 0$

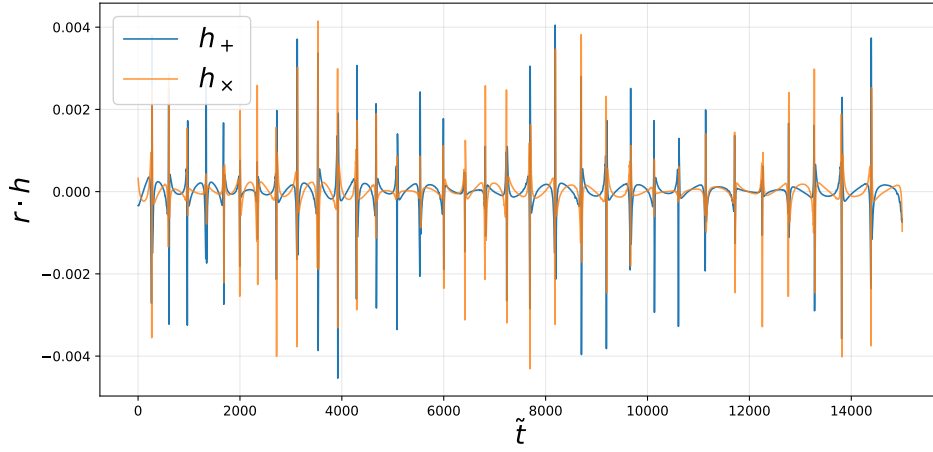


(b) $h = 0.5$

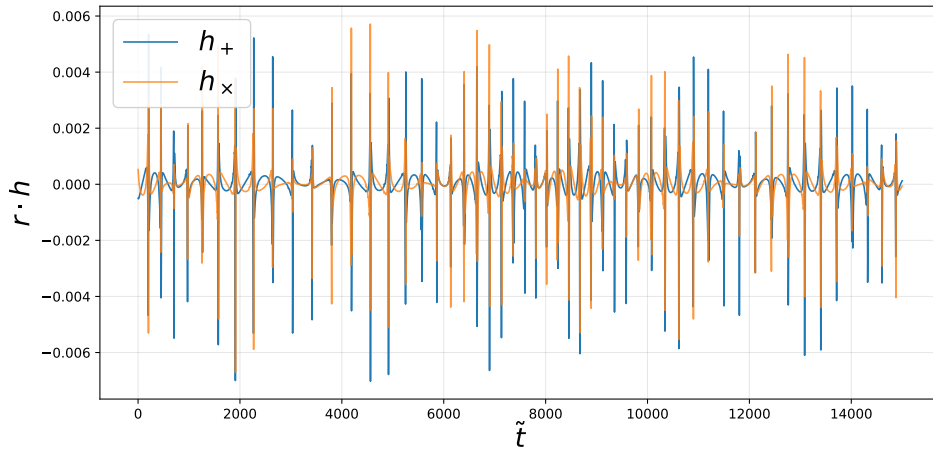


(c) $h = 1$

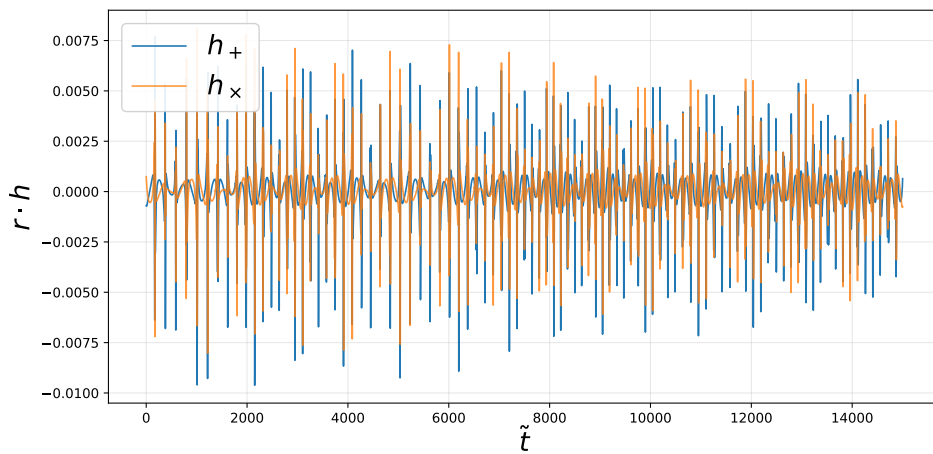
FIG. 9: Gravitational waveforms for $S = 0.5$. The blue and orange lines represent the plus polarization h_+ and the cross polarization h_\times , respectively.



(a) $h = 0$



(b) $h = 0.5$



(c) $h = 1$

FIG. 10: Gravitational waveforms for $S = 1$. The blue and orange lines represent the plus polarization h_+ and the cross polarization h_\times , respectively.

	$S = 0$		$S = 0.5$		$S = 1$	
h	CC	MAE	CC	MAE	CC	MAE
0	0.8095	0.316	0.6930	0.489	0.5011	0.490
0.5	0.8221	0.278	0.7090	0.484	0.6054	0.487
1	0.7300	0.444	0.7373	0.463	0.6914	0.460

TABLE II: CC coefficient and MAE between h_+ and h_\times ; shown for $S = 0, 0.5, 1$ and $h = 0, 0.5, 1$.

waveforms for varying spin $S = 0, 0.5, 1$ and scalar hair parameter $h = 0, 0.5, 1$ are presented Figs. 8, 9, and 10, with key statistical metrics summarized in Table II.

For a regular, nearly periodic motion, e.g., spinless particles with $S = 0$ (Fig. 8), the two polarization modes exhibit a canonical phase relationship: their signals differ only by a constant phase shift of $\frac{\pi}{2}$ [59]. This periodic structure is visually distinct across all h values, with predictable peak alignments that reflect the integrable orbital dynamics of spinless particles. Notably, even for $S = 0$, increasing h leads to a higher precession frequency, which manifests as a denser packing of waveform peaks. This change correlates with the shortened radial oscillation period observed in Fig. 4 and is consistent with the orbital dynamics analyzed in subsection IID.

For $h = 0$, introducing particle spin ($S = 0.5$ and $S = 1$) breaks the regular phase relationship between h_+ and h_\times . This is evident in the irregular peak alignment visible in Figs. 9(a) and 10(a), which signals the onset of complex dephasing. The dephasing arises directly from chaotic orbital motion driven by the spin-induced bifurcation of saddle points in the effective potential (subsection III B), a mechanism that disrupts the trajectory’s periodicity [50, 60]. Quantitatively, the dephasing is captured by the systematic decrease of the CC and increase of the MAE as the spin rises from $S = 0$ to $S = 1$. For instance, at $h = 0$ (Table II), CC drops from 0.8095 to 0.5011, while MAE rises from 0.316 to 0.490 (Table II). A similar trend occurs for $h = 0.5$.

Crucially, when $S = 1$, the physically allowed maximal spin, scalar hair h reverses this dephasing trend for chaotic systems. As h increases from 0 to 1, the CC coefficient rises monotonically from 0.5011 to 0.6914 (Table II), while the MAE decreases from 0.490 to 0.460 (Table II). This pattern confirms that stronger scalar hair aligns the two polarization modes more closely, restoring their phase coherence. The underlying physical mechanism ties back

to the chaos-suppressing effect of scalar hair: as h grows, the effective potential flattens (subsection III B), erasing saddle points, regularizing orbital precession, and reducing the chaotic divergence of trajectories (subsection IV C). This regularization of orbital dynamics directly translates to more coherent GW emissions, as the particle’s motion becomes less erratic and the polarization modes’ phase relationship stabilizes.

Notably, for $h = 1$, the CC and MAE change only slightly with spin. As shown in Table II, when S increases from 0 to 1, CC varies merely from 0.7300 to 0.6914 and MAE from 0.444 to 0.460. This insensitivity arises from the monotonic, non-restrictive form of the effective potential at large h (subsection III B), which diminishes the system’s response to spin-induced chaos. Together, these results point to a clear physical picture: the dephasing between h_+ and h_\times is driven primarily by spin-induced chaos, while scalar hair acts as a “coherence restorer” by suppressing this chaos. This distinctive GW signature could, in principle, serve as a way to detect the existence of BH scalar hair.

C. Observational Time Scales

In this subsection, we assess the observational time scales required to capture the distinctive features of the chaotic MPD system. We note that the orbital evolutions presented in this work (except Appendix B) span $N_{orbits} = 50$ orbits, a duration already sufficient to exhibit clear dephasing driven primarily by spin-induced chaos. The corresponding proper time is

$$\tau \approx 2\pi N_{orbits} \mathcal{P}^{3/2} = 111072.07345395916. \quad (52)$$

Suppose that our central object is Sgr A*, then we can calculate the proper time in physical units as follows:

$$\tau_{phys} = \beta\tau = 2.18833 \times 10^6 \text{ s} \approx 25.3279 \text{ days}, \quad (53)$$

with the transformation coefficient:

$$\beta = \frac{M_{BH}G}{c^3} = \frac{4 \times 10^6 M_{sun}G}{c^3}. \quad (54)$$

The coordinate time t , which corresponds to the actual observable duration, is listed in Table III for the maximal spin case ($S = 1$) under different hairy parameters. For the chaotic MPD system studied here, characterized by a highly spinning secondary, large an-

gular momentum, and eccentricity, the observed time scale falls below one month (26–28 days).

h	t	t_{phys} (seconds)	t_{phys} (days)
0.0	113891.95018960025	2.24388×10^6	25.9709
0.5	116726.84264158297	2.29974×10^6	26.6173
1.0	121974.18049061467	2.40312×10^6	27.8139

TABLE III: Coordinate time t in geometric and physical units for the $S = 1$ case with different hair parameters.

The relatively short time scale (weeks) identified above highlights a key advantage of chaotic MPD systems for testing fundamental physics. In standard extreme mass-ratio inspirals (EMRIs), effects beyond GR typically accumulate secularly. Confident detection often requires observational spans ranging from months to years, posing a significant challenge for the tasks of waveform modeling and data analysis [62–76]. In contrast, the chaotic orbital dynamics studied here can imprint clear dephasing signatures in the gravitational waveform within only tens of orbits. This rapid manifestation of spin-induced chaos and its suppression by scalar hair means that the “coherence–dephasing” signature discussed in subsection VB could be detectable over much shorter observational windows.

Looking forward, chaotic MPD systems could therefore serve as complementary probes to traditional EMRI campaigns. Future space-borne GW observatories such as LISA [77] may be able to identify such sources through their characteristic waveform dephasing on week-long time scales. This would open a new observational pathway to constrain scalar hair and other fundamental properties, including quantum-gravity effects.

VI. CONCLUSIONS AND DISCUSSIONS

We have studied the chaotic dynamics of a spinning test particle in the spacetime of a hairy BH within Horndeski gravity. Our central aim was to assess whether chaos can serve as a sensitive probe for detecting scalar hair. By numerically integrating the MPD equations under the TD spin condition, we analyzed the orbital morphology, LEs, Poincaré sections, and gravitational waveforms for various values of the hair parameter h .

Our results demonstrate that the presence of scalar hair systematically suppresses chaotic behavior. As h increases, the effective potential becomes shallower, reducing radial confinement and regularizing the orbital precession. This is reflected in the shrinkage of the Lorenz attractor, the consolidation of Poincaré sections into tighter regions, and a clear decrease in the maximal LE. These indicators collectively show that scalar hair acts as a damping agent on chaotic spin-curvature coupling. Furthermore, we extended the analysis to the gravitational waveform emitted by the spinning particle, constructed via the quadrupole formula. We found that increasing h enhances the correlation between the two polarization modes h_+ and h_\times , as quantified by CC and MAE. This indicates that scalar hair not only regularizes the orbital dynamics but also restores phase coherence in the GW signal, providing a complementary observable for testing deviations from GR.

Our work demonstrates that chaotic dynamics can act as a natural amplifier for faint gravitational hair. Minute deviations in the metric, which would be exceedingly difficult to detect in regular, integrable motion, are magnified into clear and quantifiable differences in chaotic indicators and waveform morphology. This establishes chaotic observables—accessible via the orbital monitoring of stars near supermassive BHs or via the gravitational waveforms of inspiraling compact objects—as a powerful complementary tool for testing strong-field gravity. In regimes where weak-field solar-system tests are saturated, the chaotic amplification of hair-related effects offers a novel pathway to detection.

Future work should extend this framework to rotating hairy BHs, where spin–spin interactions could further modulate chaos, and to more general Horndeski couplings. Investigating how these effects imprint on the GW strain detectable by LISA, Einstein Telescope, or Cosmic Explorer will be essential for connecting our theoretical findings to future astrophysical observations.

Acknowledgments

We are especially grateful to Guoyang Fu for his valuable discussions. Yang Yu also wishes to thank Rui Bo and Qiaonan Li for their essential help with programming. This work is supported by the Natural Science Foundation of China under Grant Nos. 12375055, 12505085, the Jiangsu Postgraduate Research and Practice Innovation Program under Grant No. KYCX25_3925, the China Postdoctoral Science Foundation (No. 2025T180931), and

the Jiangsu Funding Program for Excellent Postdoctoral Talent (No. 2025ZB705).

Appendix A: Energy and Angular Momentum in Terms of Orbital Parameters

To obtain the energy E and the angular momentum L_z in terms of the orbital parameters \mathcal{P} , e , and θ_m , we need to solving the following equations [51, 52]:

$$R(r) = 0, \quad (\text{A1a})$$

$$\Theta(\theta) = 0, \quad (\text{A1b})$$

where $R(r)$ and $\Theta(\theta)$ are given by Eqs. (14a) and (14b), respectively. Their solutions are associated with the turning points of radial and polar motion. We can insert

$$r_p = \frac{\mathcal{P}}{1+e}, \quad (\text{A2a})$$

$$r_a = \frac{\mathcal{P}}{1-e}, \quad (\text{A2b})$$

into Eq. (A1a) and $\theta = \theta_m$ into Eq. (A1b). If $e \neq 0$, then we have a set of equations with three unknown constants of motion. For $e = 0$, an additional condition $R'(r) = 0$ is required, as circular orbits occur when both $R(r)$ and $R'(r)$ vanish at $r = r_0$.

Substituting Eq. (17) into Eq. (14a) gives, for a spherical spacetime,

$$R(r) = \tilde{f}(r)E^2 - 2\tilde{g}(r)EL_z - \tilde{h}(r)L_z^2 - \tilde{d}(r), \quad (\text{A3})$$

where

$$\tilde{f}(r) = r^4, \quad (\text{A4a})$$

$$\tilde{g}(r) = 0, \quad (\text{A4b})$$

$$\tilde{h}(r) = r^2 f(r) \left(1 + \frac{z_m^2}{1-z_m^2} \right), \quad (\text{A4c})$$

$$\tilde{d}(r) = r^4 f(r), \quad (\text{A4d})$$

and $f(r)$ is the metric function from Eq. (2). The derivative $R'(r)$ is

$$R'(r) = \tilde{f}'(r)E^2 - 2\tilde{g}'(r)EL_z - \tilde{h}'(r) - \tilde{d}'(r), \quad (\text{A5})$$

with

$$\tilde{f}'(r) = 4r^3, \quad (\text{A6a})$$

$$\tilde{g}'(r) = 0, \quad (\text{A6b})$$

$$\tilde{h}'(r) = r[2f(r) + rf'(r)] \left(1 - \frac{z_m^2}{1 - z_m^2}\right), \quad (\text{A6c})$$

$$\tilde{d}'(r) = 4r^3 f(r) + r^4 f'(r). \quad (\text{A6d})$$

The coefficients can therefore be expressed in terms of the orbital parameters. When $e > 0$, they are

$$(\tilde{f}_1, \tilde{g}_1, \tilde{h}_1, \tilde{d}_1) = (\tilde{f}(r_p), \tilde{g}(r_p), \tilde{h}(r_p), \tilde{d}(r_p)), \quad (\text{A7a})$$

$$(\tilde{f}_2, \tilde{g}_2, \tilde{h}_2, \tilde{d}_2) = (\tilde{f}(r_a), \tilde{g}(r_a), \tilde{h}(r_a), \tilde{d}(r_a)). \quad (\text{A7b})$$

When $e = 0$, they become

$$(\tilde{f}_1, \tilde{g}_1, \tilde{h}_1, \tilde{d}_1) = (\tilde{f}(r_0), \tilde{g}(r_0), \tilde{h}(r_0), \tilde{d}(r_0)), \quad (\text{A8a})$$

$$(\tilde{f}'_2, \tilde{g}'_2, \tilde{h}'_2, \tilde{d}'_2) = (\tilde{f}'(r_0), \tilde{g}'(r_0), \tilde{h}'(r_0), \tilde{d}'(r_0)). \quad (\text{A8b})$$

Then, E and L_z can be determined from the following equations:

$$\tilde{f}_1 E^2 - 2\tilde{g}_1 E L_z - \tilde{h}_1 L_z^2 - \tilde{d}_1 = 0, \quad (\text{A9a})$$

$$\tilde{f}_2 E^2 - 2\tilde{g}_2 E L_z - \tilde{h}_2 L_z^2 - \tilde{d}_2 = 0, \quad (\text{A9b})$$

whose solutions are

$$E = \sqrt{\frac{\mathbf{ac} + 2\mathbf{be} - 2 \pm \sqrt{\mathbf{e}(\mathbf{eb}^2 + \mathbf{cba} - \mathbf{da}^2)}}{\mathbf{c}^2 + 4\mathbf{de}}}, \quad (\text{A10a})$$

$$L_z = -\frac{\tilde{g}_1}{\tilde{h}_1} E \pm \frac{1}{\tilde{h}_1} \sqrt{\tilde{g}_1^2 E^2 + (\tilde{f}_1 E^2 + \tilde{d}_1) \tilde{h}_1}, \quad (\text{A10b})$$

with

$$\mathbf{a} = \tilde{d}_1 \tilde{h}_2 - \tilde{d}_2 \tilde{h}_1, \quad (\text{A11a})$$

$$\mathbf{b} = \tilde{d}_1 \tilde{g}_2 - \tilde{d}_2 \tilde{g}_1, \quad (\text{A11b})$$

$$\mathbf{c} = \tilde{f}_1 \tilde{h}_2 - \tilde{f}_2 \tilde{h}_1, \quad (\text{A11c})$$

$$\mathbf{d} = \tilde{f}_1 \tilde{g}_2 - \tilde{f}_2 \tilde{g}_1, \quad (\text{A11d})$$

$$\mathbf{e} = \tilde{g}_1 \tilde{h}_2 - \tilde{g}_2 \tilde{h}_1. \quad (\text{A11e})$$

Appendix B: The Poincaré Section in An Extremely Long Time Evolution

In Sec. IV, we observe that the Poincaré section shows a fractal structure over sufficiently long evolution time. Since our primary goal is to investigate how the hairy parameter h influences chaotic behavior, we focus on the most chaotic scenario. However, generating a Poincaré section with a fractal structure requires a system exhibiting moderate chaos. This is because, in such a system, a particle will neither be scattered nor fall into the BH over extremely long time scales. These two requirements are inherently contradictory. Moreover, the extreme cases discussed in Sec. III do not allow such long-term evolution. In contrast to the scenario investigated in the main body, we adopt a new set of parameters $(S, h, e) = (0.8096, 1, 0.2)$ to simulate the system over a substantially longer duration, in which the fractal structure emerges (Fig. 11).

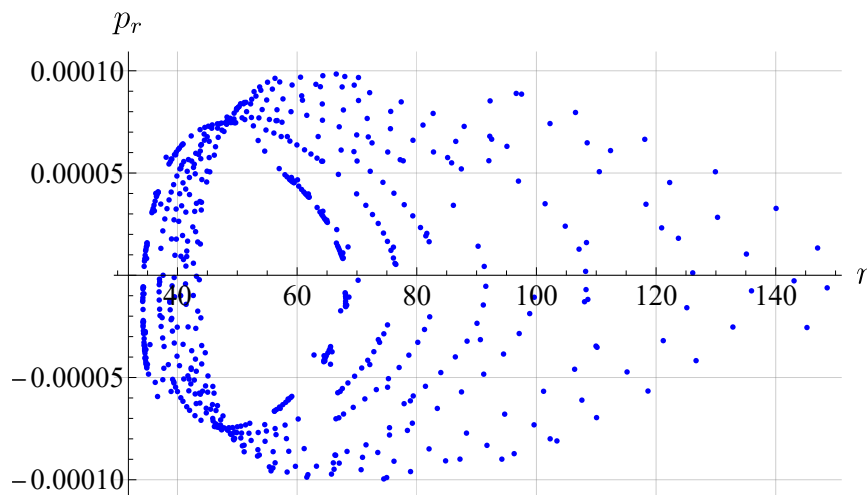


FIG. 11: The Poincaré section in long time evolution.

-
- [1] M. Heusler, “No hair theorems and black holes with hair,” *Helv. Phys. Acta* **69** no. 4, (1996) 501–528, [arXiv:gr-qc/9610019](#).
 - [2] D. C. Robinson, “Uniqueness of the Kerr black hole,” *Phys. Rev. Lett.* **34** (1975) 905–906.
 - [3] P. T. Chrusciel, J. Lopes Costa, and M. Heusler, “Stationary Black Holes: Uniqueness and Beyond,” *Living Rev. Rel.* **15** (2012) 7, [arXiv:1205.6112 \[gr-qc\]](#).

- [4] B. Carter, “Axisymmetric Black Hole Has Only Two Degrees of Freedom,” [Phys. Rev. Lett.](#) **26** (1971) 331–333.
- [5] S. W. Hawking, “Black holes in general relativity,” [Commun. Math. Phys.](#) **25** (1972) 152–166.
- [6] R. Kase and S. Tsujikawa, “Dark energy in Horndeski theories after GW170817: A review,” [Int. J. Mod. Phys. D](#) **28** no. 05, (2019) 1942005, [arXiv:1809.08735 \[gr-qc\]](#).
- [7] C. M. Will, “The Confrontation between General Relativity and Experiment,” [Living Rev. Rel.](#) **17** (2014) 4, [arXiv:1403.7377 \[gr-qc\]](#).
- [8] **LIGO Scientific, Virgo** Collaboration, B. P. Abbott *et al.*, “Tests of general relativity with GW150914,” [Phys. Rev. Lett.](#) **116** no. 22, (2016) 221101, [arXiv:1602.03841 \[gr-qc\]](#). [Erratum: Phys.Rev.Lett. 121, 129902 (2018)].
- [9] **LIGO Scientific, Virgo** Collaboration, B. P. Abbott *et al.*, “GW151226: Observation of Gravitational Waves from a 22-Solar-Mass Binary Black Hole Coalescence,” [Phys. Rev. Lett.](#) **116** no. 24, (2016) 241103, [arXiv:1606.04855 \[gr-qc\]](#).
- [10] **LIGO Scientific, Virgo** Collaboration, B. P. Abbott *et al.*, “Tests of General Relativity with the Binary Black Hole Signals from the LIGO-Virgo Catalog GWTC-1,” [Phys. Rev. D](#) **100** no. 10, (2019) 104036, [arXiv:1903.04467 \[gr-qc\]](#).
- [11] S. Suzuki and K.-i. Maeda, “Chaos in Schwarzschild space-time: The motion of a spinning particle,” [Phys. Rev. D](#) **55** (1997) 4848–4859, [arXiv:gr-qc/9604020](#).
- [12] M. Mathisson, “Neue mechanik materieller systemes,” [Acta Phys. Polon.](#) **6** (1937) 163–200.
- [13] A. Papapetrou, “Spinning test particles in general relativity. 1.,” [Proc. Roy. Soc. Lond. A](#) **209** (1951) 248–258.
- [14] W. G. Dixon, “Dynamics of extended bodies in general relativity. I. Momentum and angular momentum,” [Proc. Roy. Soc. Lond. A](#) **314** (1970) 499–527.
- [15] **Event Horizon Telescope** Collaboration, K. Akiyama *et al.*, “First M87 Event Horizon Telescope Results. I. The Shadow of the Supermassive Black Hole,” [Astrophys. J. Lett.](#) **875** (2019) L1, [arXiv:1906.11238 \[astro-ph.GA\]](#).
- [16] **Event Horizon Telescope** Collaboration, K. Akiyama *et al.*, “First M87 Event Horizon Telescope Results. VI. The Shadow and Mass of the Central Black Hole,” [Astrophys. J. Lett.](#) **875** no. 1, (2019) L6, [arXiv:1906.11243 \[astro-ph.GA\]](#).
- [17] **Event Horizon Telescope** Collaboration, K. Akiyama *et al.*, “First M87 Event Horizon

- Telescope Results. III. Data Processing and Calibration,” [Astrophys. J. Lett.](#) **875** no. 1, (2019) L3, [arXiv:1906.11240](#) [astro-ph.GA].
- [18] **Event Horizon Telescope** Collaboration, K. Akiyama *et al.*, “First M87 Event Horizon Telescope Results. V. Physical Origin of the Asymmetric Ring,” [Astrophys. J. Lett.](#) **875** no. 1, (2019) L5, [arXiv:1906.11242](#) [astro-ph.GA].
- [19] **Event Horizon Telescope** Collaboration, K. Akiyama *et al.*, “First M87 Event Horizon Telescope Results. IV. Imaging the Central Supermassive Black Hole,” [Astrophys. J. Lett.](#) **875** no. 1, (2019) L4, [arXiv:1906.11241](#) [astro-ph.GA].
- [20] **Event Horizon Telescope** Collaboration, K. Akiyama *et al.*, “First M87 Event Horizon Telescope Results. II. Array and Instrumentation,” [Astrophys. J. Lett.](#) **875** no. 1, (2019) L2, [arXiv:1906.11239](#) [astro-ph.IM].
- [21] **Event Horizon Telescope** Collaboration, K. Akiyama *et al.*, “First Sagittarius A* Event Horizon Telescope Results. II. EHT and Multiwavelength Observations, Data Processing, and Calibration,” [Astrophys. J. Lett.](#) **930** no. 2, (2022) L13.
- [22] **Event Horizon Telescope** Collaboration, K. Akiyama *et al.*, “First Sagittarius A* Event Horizon Telescope Results. IV. Variability, Morphology, and Black Hole Mass,” [Astrophys. J. Lett.](#) **930** no. 2, (2022) L15.
- [23] **Event Horizon Telescope** Collaboration, K. Akiyama *et al.*, “First Sagittarius A* Event Horizon Telescope Results. V. Testing Astrophysical Models of the Galactic Center Black Hole,” [Astrophys. J. Lett.](#) **930** no. 2, (2022) L16.
- [24] **Event Horizon Telescope** Collaboration, K. Akiyama *et al.*, “First Sagittarius A* Event Horizon Telescope Results. III. Imaging of the Galactic Center Supermassive Black Hole,” [Astrophys. J. Lett.](#) **930** no. 2, (2022) L14.
- [25] **Event Horizon Telescope** Collaboration, K. Akiyama *et al.*, “First Sagittarius A* Event Horizon Telescope Results. VI. Testing the Black Hole Metric,” [Astrophys. J. Lett.](#) **930** no. 2, (2022) L17.
- [26] **LIGO Scientific, Virgo** Collaboration, B. P. Abbott *et al.*, “GW150914: The Advanced LIGO Detectors in the Era of First Discoveries,” [Phys. Rev. Lett.](#) **116** no. 13, (2016) 131103, [arXiv:1602.03838](#) [gr-qc].
- [27] **LIGO Scientific, Virgo** Collaboration, B. P. Abbott *et al.*, “GW150914: First results from the search for binary black hole coalescence with Advanced LIGO,” [Phys. Rev. D](#) **93** no. 12,

- (2016) 122003, [arXiv:1602.03839 \[gr-qc\]](#).
- [28] **LIGO Scientific, Virgo** Collaboration, B. P. Abbott *et al.*, “Properties of the Binary Black Hole Merger GW150914,” [Phys. Rev. Lett.](#) **116** no. 24, (2016) 241102, [arXiv:1602.03840 \[gr-qc\]](#).
- [29] **LIGO Scientific, Virgo** Collaboration, B. P. Abbott *et al.*, “Astrophysical Implications of the Binary Black-Hole Merger GW150914,” [Astrophys. J. Lett.](#) **818** no. 2, (2016) L22, [arXiv:1602.03846 \[astro-ph.HE\]](#).
- [30] **LIGO Scientific, VIRGO** Collaboration, B. P. Abbott *et al.*, “GW170104: Observation of a 50-Solar-Mass Binary Black Hole Coalescence at Redshift 0.2,” [Phys. Rev. Lett.](#) **118** no. 22, (2017) 221101, [arXiv:1706.01812 \[gr-qc\]](#). [Erratum: Phys.Rev.Lett. 121, 129901 (2018)].
- [31] **LIGO Scientific, Virgo** Collaboration, B. P. Abbott *et al.*, “GWTC-1: A Gravitational-Wave Transient Catalog of Compact Binary Mergers Observed by LIGO and Virgo during the First and Second Observing Runs,” [Phys. Rev. X](#) **9** no. 3, (2019) 031040, [arXiv:1811.12907 \[astro-ph.HE\]](#).
- [32] M. Isi, M. Giesler, W. M. Farr, M. A. Scheel, and S. A. Teukolsky, “Testing the no-hair theorem with GW150914,” [Phys. Rev. Lett.](#) **123** no. 11, (2019) 111102, [arXiv:1905.00869 \[gr-qc\]](#).
- [33] T. Johannsen and D. Psaltis, “Testing the No-Hair Theorem with Observations in the Electromagnetic Spectrum: II. Black-Hole Images,” [Astrophys. J.](#) **718** (2010) 446–454, [arXiv:1005.1931 \[astro-ph.HE\]](#).
- [34] T. Johannsen and D. Psaltis, “A Metric for Rapidly Spinning Black Holes Suitable for Strong-Field Tests of the No-Hair Theorem,” [Phys. Rev. D](#) **83** (2011) 124015, [arXiv:1105.3191 \[gr-qc\]](#).
- [35] M. Khodadi, A. Allahyari, S. Vagnozzi, and D. F. Mota, “Black holes with scalar hair in light of the Event Horizon Telescope,” [JCAP](#) **09** (2020) 026, [arXiv:2005.05992 \[gr-qc\]](#).
- [36] A. E. Broderick, T. Johannsen, A. Loeb, and D. Psaltis, “Testing the No-Hair Theorem with Event Horizon Telescope Observations of Sagittarius A*,” [Astrophys. J.](#) **784** (2014) 7, [arXiv:1311.5564 \[astro-ph.HE\]](#).
- [37] E. Babichev, C. Charmousis, and A. Lehébel, “Asymptotically flat black holes in Horndeski theory and beyond,” [JCAP](#) **04** (2017) 027, [arXiv:1702.01938 \[gr-qc\]](#).

- [38] S. E. P. Bergliaffa, R. Maier, and N. d. O. Silvano, “Hairy Black Holes from Horndeski Theory,” [arXiv:2107.07839 \[gr-qc\]](#).
- [39] X.-J. Wang, X.-M. Kuang, Y. Meng, B. Wang, and J.-P. Wu, “Rings and images of Horndeski hairy black hole illuminated by various thin accretions,” [Phys. Rev. D](#) **107** no. 12, (2023) 124052, [arXiv:2304.10015 \[gr-qc\]](#).
- [40] Z.-H. Yang, Y.-H. Lei, X.-M. Kuang, and J.-P. Wu, “Perturbations of massless external fields in a special Horndeski hairy black hole,” [Eur. Phys. J. C](#) **84** no. 2, (2024) 153, [arXiv:2309.03565 \[gr-qc\]](#).
- [41] J. Kumar, S. U. Islam, and S. G. Ghosh, “Investigating strong gravitational lensing effects by supermassive black holes with Horndeski gravity,” [Eur. Phys. J. C](#) **82** no. 5, (2022) 443, [arXiv:2109.04450 \[gr-qc\]](#).
- [42] R. K. Walia, S. D. Maharaj, and S. G. Ghosh, “Rotating Black Holes in Horndeski Gravity: Thermodynamic and Gravitational Lensing,” [Eur. Phys. J. C](#) **82** (2022) 547, [arXiv:2109.08055 \[gr-qc\]](#).
- [43] M. Afrin and S. G. Ghosh, “Testing Horndeski Gravity from EHT Observational Results for Rotating Black Holes,” [Astrophys. J.](#) **932** no. 1, (2022) 51, [arXiv:2110.05258 \[gr-qc\]](#).
- [44] H.-Y. Lin and X.-M. Deng, “Precessing and periodic orbits around hairy black holes in Horndeski’s Theory,” [Eur. Phys. J. C](#) **83** no. 4, (2023) 311.
- [45] S. K. Jha, M. Khodadi, A. Rahaman, and A. Sheykhi, “Superradiant energy extraction from rotating hairy Horndeski black holes,” [Phys. Rev. D](#) **107** no. 8, (2023) 084052, [arXiv:2212.13051 \[gr-qc\]](#).
- [46] S. G. Ghosh and M. Afrin, “An Upper Limit on the Charge of the Black Hole Sgr A* from EHT Observations,” [Astrophys. J.](#) **944** no. 2, (2023) 174, [arXiv:2206.02488 \[gr-qc\]](#).
- [47] V. Witzany, J. Steinhoff, and G. Lukes-Gerakopoulos, “Hamiltonians and canonical coordinates for spinning particles in curved space-time,” [Class. Quant. Grav.](#) **36** no. 7, (2019) 075003, [arXiv:1808.06582 \[gr-qc\]](#).
- [48] W. Tulczyjew, “Motion of multipole particles in general relativity theory,” [Acta Phys. Pol](#) **18** no. 393, (1959) 94.
- [49] K. P. Tod, F. de Felice, and M. Calvani, “Spinning test particles in the field of a black hole,” [Nuovo Cim. B](#) **34** (1976) 365.
- [50] D. Singh, “The Dynamics of a classical spinning particle in Vaidya space-time,” [Phys. Rev.](#)

- [D 72](#) (2005) 084033, [arXiv:gr-qc/0509046](#).
- [51] T. Kimpson, K. Wu, and S. Zane, “Orbital spin dynamics of a millisecond pulsar around a massive BH with a general mass quadrupole,” [Monthly Notices of the Royal Astronomical Society](#) **497** no. 4, (Aug., 2020) 5421–5431. <https://doi.org/10.1093/mnras/staa2103>.
eprint: <https://academic.oup.com/mnras/article-pdf/497/4/5421/33695867/staa2103.pdf>.
- [52] W. Schmidt, “Celestial mechanics in Kerr space-time,” [Class. Quant. Grav.](#) **19** (2002) 2743, [arXiv:gr-qc/0202090](#).
- [53] B. Mashhoon and D. Singh, “Dynamics of Extended Spinning Masses in a Gravitational Field,” [Phys. Rev. D](#) **74** (2006) 124006, [arXiv:astro-ph/0608278](#).
- [54] S. Chandrasekhar, [The mathematical theory of black holes](#), vol. 69. Oxford university press, 1998.
- [55] J. Botvinick-Greenhouse, M. Oprea, R. Maulik, and Y. Yang, “Measure-theoretic time-delay embedding,” [arXiv preprint arXiv:2409.08768](#) (2024) .
- [56] M. Sano and Y. Sawada, “Measurement of the lyapunov spectrum from a chaotic time series,” [Physical review letters](#) **55** no. 10, (1985) 1082.
- [57] A. Wolf, J. B. Swift, H. L. Swinney, and J. A. Vastano, “Determining lyapunov exponents from a time series,” [Physica D: nonlinear phenomena](#) **16** no. 3, (1985) 285–317.
- [58] E. Poisson and C. M. Will, [Gravity: Newtonian, post-newtonian, relativistic](#). Cambridge University Press, 2014.
- [59] M. Maggiore, [Gravitational waves: Volume 1: Theory and experiments](#), vol. 1. Oxford university press, 2008.
- [60] S. Suzuki and K.-i. Maeda, “Signature of chaos in gravitational waves from a spinning particle,” [Phys. Rev. D](#) **61** (2000) 024005, [arXiv:gr-qc/9910064](#).
- [61] K. M. Keita, “Machine learning complete intersection Calabi-Yau 3-folds,” [Phys. Rev. D](#) **110** no. 12, (2024) 126002, [arXiv:2404.11710 \[hep-th\]](#).
- [62] S. A. Hughes, N. Warburton, G. Khanna, A. J. K. Chua, and M. L. Katz, “Adiabatic waveforms for extreme mass-ratio inspirals via multivoice decomposition in time and frequency,” [Phys. Rev. D](#) **103** no. 10, (2021) 104014, [arXiv:2102.02713 \[gr-qc\]](#).
[Erratum: [Phys.Rev.D](#) 107, 089901 (2023)].
- [63] B. Wardell, A. Pound, N. Warburton, J. Miller, L. Durkan, and A. Le Tiec, “Gravitational Waveforms for Compact Binaries from Second-Order Self-Force Theory,” [Phys. Rev. Lett.](#)

- 130** no. 24, (2023) 241402, [arXiv:2112.12265 \[gr-qc\]](#).
- [64] H. Iglesias, L. Durkan, and D. Shoemaker, “Hybridization of second-order gravitational self-force and numerical relativity waveforms for quasi-circular and non-spinning black hole binaries,” [arXiv:2510.11685 \[gr-qc\]](#).
- [65] C. Zhang, R.-g. Cai, G. Fu, Y. Gong, X. Lu, and W. Zhou, “Generic effective sources for first-order in mass-ratio gravitational self-force calculations in Schwarzschild spacetime,” [Phys. Rev. D **112** no. 10, \(2025\) 104069, arXiv:2505.19732 \[gr-qc\]](#).
- [66] Y.-X. Wei, X.-L. Zhu, J.-d. Zhang, and J. Mei, “Toward second-order self-force for eccentric extreme-mass ratio inspirals in Schwarzschild spacetimes,” [Phys. Rev. D **112** no. 6, \(2025\) 064048, arXiv:2504.09640 \[gr-qc\]](#).
- [67] J. R. Gair, E. K. Porter, S. Babak, and L. Barack, “A Constrained Metropolis-Hastings Search for EMRIs in the Mock LISA Data Challenge 1B,” [Class. Quant. Grav. **25** \(2008\) 184030, arXiv:0804.3322 \[gr-qc\]](#).
- [68] **Mock LISA Data Challenge Task Force** Collaboration, S. Babak *et al.*, “The Mock LISA Data Challenges: From Challenge 3 to Challenge 4,” [Class. Quant. Grav. **27** \(2010\) 084009, arXiv:0912.0548 \[gr-qc\]](#).
- [69] **LDC Working Group** Collaboration, Q. Baghi, “The LISA Data Challenges,” in [56th Rencontres de Moriond on Gravitation](#). 4, 2022. [arXiv:2204.12142 \[gr-qc\]](#).
- [70] E.-K. Li *et al.*, “Gravitational wave astronomy with TianQin,” [Rept. Prog. Phys. **88** no. 5, \(2025\) 056901, arXiv:2409.19665 \[astro-ph.GA\]](#).
- [71] H.-M. Fan, Y.-M. Hu, E. Barausse, A. Sesana, J.-d. Zhang, X. Zhang, T.-G. Zi, and J. Mei, “Science with the TianQin observatory: Preliminary result on extreme-mass-ratio inspirals,” [Phys. Rev. D **102** no. 6, \(2020\) 063016, arXiv:2005.08212 \[astro-ph.HE\]](#).
- [72] L. Speri, R. Tenorio, C. Chapman-Bird, and D. Gerosa, “Ab uno disce omnes: Single-harmonic search for extreme mass-ratio inspirals,” [arXiv:2510.20891 \[gr-qc\]](#).
- [73] Z. Xiaobo *et al.*, “An Overview of EMRI Data Analysis,” [Acta Sci. Natur. Univ. Pekin. **61** no. no. 1 \(2025\): 181-194, \(2025\) 13](#).
- [74] H. Gong, S. Long, X.-J. Wang, Z. Xia, J.-P. Wu, and Q. Pan, “Gravitational waveforms from periodic orbits around a novel regular black hole,” [arXiv:2509.23318 \[gr-qc\]](#).
- [75] G. Fu, Y. Liu, B. Wang, J.-P. Wu, and C. Zhang, “Probing quantum gravity effects with eccentric extreme mass-ratio inspirals,” [Phys. Rev. D **111** no. 8, \(2025\) 084066](#),

[arXiv:2409.08138](#) [gr-qc].

- [76] R.-T. Chen, G. Fu, D. Zhang, and J.-P. Wu, “Imprints of quantum gravity effects on gravitational waves: a comparative study using extreme mass-ratio inspirals,”

[arXiv:2601.00185](#) [gr-qc].

- [77] **LISA** Collaboration, K. G. Arun et al., “New horizons for fundamental physics with LISA,”

[Living Rev. Rel.](#) **25** no. 1, (2022) 4, [arXiv:2205.01597](#) [gr-qc].